Experimental evaluation of modular antenna arrays at 28 GHz under the presence of human body

Lauri Vähä-Savo

School of Electrical Engineering

Thesis submitted for examination for the degree of Master of Science in Technology.

Espoo 30.9.2019

Supervisor

Prof. Katsuyuki Haneda

Advisor

D.Sc. (Tech) Clemens Icheln

Aalto University
School of Electrical
Engineering

Aalto University
School of Electrical
Engineering

Aalto University, P.O. BOX 11000, 00076 AALTO
www.aalto.fi
Abstract of the master's thesis

Author Lauri Vähä-Savo

Title Experimental evaluation of modular antenna arrays at 28 GHz under the presence of human body

Degree programme Electronics and electrical engineering

Major Radio Science and Engineering **Code of major** ELEC3038

Supervisor Prof. Katsuyuki Haneda

Advisor D.Sc. (Tech) Clemens Icheln

Date 30.9.2019 **Number of pages** 59+13 **Language** English

Abstract

The goal of this thesis is to develop and test an experimental method for characterising antenna arrays for mobile phones at 28 GHz under the presence of the user. Previous studies were based merely on computer simulations, or on measurements with actual humans, where repeatability is an unsolved issue. Antenna measurements with a human phantom have now been carried out and analysed for the first time. For their validation, simulation methods for characterising mm-wave mobile phone antennas under the presence of a human body, and the detailed evaluation process are presented here, including spherical coverage and total array gain.

Utilising the presented simulation methods, a simplified human phantom is designed, validated, and manufactured. The electrical properties of human tissues are well known, and different material recipes to mimic human skin were reported in previous studies. Based on these, we created a polyethylene-based skin-like material with electrical properties similar as in human skin. This material was used as a surface for the final human phantom. This phantom was then used in radiation-pattern measurements at 28 GHz. Two planar 2×2 dual-polarised antenna arrays were designed and manufactured. As expected, the design of the microstrip-feed line network was crucial in the design of the antenna arrays, especially the mutual coupling needs to be low to ensure the designed operation of the arrays. Antenna radiation pattern measurements, both in free space and with the human phantom, were carried out in an anechoic chamber. The losses of feed cables and connectors were de-embedded by calculating suitable amplitude correction terms that normalize differences between measured and simulated free-space element patterns. The phantom measurements were performed with both antenna arrays, and after mathematical beam-forming with a suitable amount of element-phasing cases, the spherical coverage of each array was calculated. Element radiation patterns and spherical coverage of both antenna arrays under the presence of the human phantom were compared to the simulations. In the spherical coverage CDFs of both arrays, the difference between measured and simulated peak gain is 1 - 2 dB, and the difference between measured and simulated median gain level is 0.6 - 2 dB. This comparison shows that the proposed experimental method for characterising mm-wave mobile antenna arrays in the presence of the user is feasible. One test array also was measured twice with the phantom and the maximum difference between spherical coverage CDFs was 1 dB proving good repeatability of the proposed experimental method.

Keywords Mobile antennas, Human phantom, Skin material, Antenna evaluation, Millimeter waves

Aalto University
School of Electrical Engineering

Aalto-yliopisto, PL 11000, 00076 AALTO
www.aalto.fi
Diplomityön tiivistelmä

Tekijä Lauri Vähä-Savo

Työn nimi Modulaaristen antenni ryhmien kokeellinen arviointi ihmisen läheisyydessä 28 GHz taajuudella

Koulutusohjelma Nano- ja radiotieteiden maisteriohjelma

Pääaine Radiotiede ja -tekniikka **Pääaineen koodi** ELEC3038

Työn valvoja Prof. Katsuyuki Haneda

Työn ohjaaja TkT Clemens Icheln

Päivämäärä 30.9.2019 **Sivumäärä** 59+13 **Kieli** Englanti

Tiivistelmä

Tämän työn tarkoituksena on kehittää ja testata kokeellista menetelmää matkapuhelimien antenniryhmien karakterisoimiseksi 28 GHz taajuudella käyttäjän läheisyydessä. Aikaisemmat tutkimukset ovat olleet lähinnä tietokoneella tehtyjä simulaatioita tai mittauksia joissa on käytetty oikeita ihmisiä. Näissä mittauskokeissa toistettavuus on ratkaisematon ongelma. Tässä työssä toteutetut antenni mittaukset ihmismallinuken kanssa ovat ensimmäiset laatuaan. Mittausten tueksi esitetään simulaatiomenetelmät mm-aalto matkapuhelin antennien karakterisoimiseksi ihmiskehon läsnä ollessa ja yksityiskohtainen arviointiprosessi, mukaan lukien pallopinnan peiton (spherical coverage) ja kokonaisryhmävahvistuksen (total array gain).

Esitettyjä simulaatiomenetelmiä hyödyntäen suunnitellaan, validoidaan ja valmistetaan yksinkertaistettu ihmismallinukke. Ihmiskudosten sähköiset ominaisuudet ovat hyvin tunnettuja, ja erilaisia reseptejä materiaaleille jotka jäljittelevät ihmisen ihoa on raportoitu aiemmissa tutkimuksissa. Näiden perusteella loimme polyeteenipohjaisen ihoa jäljittelevän materiaalin, jonka sähköiset ominaisuudet ovat samanlaiset kuin ihmisen iholla. Tätä materiaalia käytettiin lopullisen ihmismallinuken pintana. Tätä mallinukkea käytettiin säteilykuviomittauksissa 28 GHz:n taajuudella. Mittauksia varten suunniteltiin ja valmistettiin kaksi tasomaista 2×2 kaksoispolarisoitua antenniryhmää. Syöttöjohtoverkon suunnittelu on tärkeä antenniryhmien suunnittelussa, etenkin keskinäisen kytkennän on oltava alhainen ryhmien suunnitellun toiminnan varmistamiseksi. Antennien säteilykuvion mittaukset, sekä vapaassa tilassa että ihmismallinuken kanssa, suoritettiin kaiutumattomassa kammiossa. Syöttökaapeleiden ja liittimien häviöt tasoitettiin laskemalla sopivat amplitudikorjauskertoimet, jotka normalisoivat mitatun ja simuloidun vapaan tilan elementtikuvioiden väliset erot. Mittaukset mallinuken kanssa suoritettiin molemmilla antenniryhmillä, jonka jälkeen toteutettiin matemaattinen säteenmuodostus sopivalla määrällä elementtivaihetapauksia ja laskettiin kunkin ryhmän pallopinnan peitto. Molempien antenniryhmien elementtien säteilykuvioita ja pallopinnan peittoa ihmismallinuken läsnä ollessa verrattiin simulaatioihin. Molempien ryhmien pallopinnan peiton-CDF:issä mitatun ja simuloidun piikinvahvistuksen välinen ero on 1 - 2 dB ja ero mitatun ja simuloidun välillä mediaanitasolla on 0,6 - 2 dB. Tämä vertailu osoittaa, että ehdotettu kokeellinen menetelmä mm-aaltojen matkapuhelinantenniryhmien karakterisoimiseksi käyttäjän läsnä ollessa on toteutettavissa. Yksi testiryhmä mitattiin myös kahdesti mallinuken kanssa ja pallopinnan peiton CDF:ien suurin ero oli 1 dB, mikä osoitti esitetyn kokeellisen menetelmän hyvän toistettavuuden.

Avainsanat Matkapuhelin antennit, Ihmismallinukke, Ihomateriaali, Antennien arviointi, millimetri aallot

Preface

The research for this thesis was carried out at the Department of Electronics and Nanoengineering in Aalto University School of Electrical Engineering under supervision of Prof. Katsuyuki Haneda who I like thank for great guidance not only during this thesis but also during my whole master studies. I would like thank also my advisor D.Sc. (Tech) Clemens Icheln, without his intelligent ideas this thesis would still be work in progress. Huawei Technologies Oy funded and steered this project. From Huawei I like to thank especially Ali Hazmi and Ruiyuan Tian of their ideas, interest and steering during this project.

During my time in Otaniemi, I have had privilege to learn and do much more than just 300 cr. which university demands. First of all I like to thank Guild of Electrical Engineering, SIKH14 and SIKH15 from experiences and memories that I got during my studies. Also FTMK15 is part of those memories that won't fade away. However, if this was not enough I have had privilege to be part of groups/clubs/tribes and events during all these years. Jalostajat has gave me opportunity to work with multiple projects from craft bear festivals to washing dishes. In Luola, under supervision of Nasku and Jubileum, I have been part of making the world more fun place. Well, at least we tried. So thank you Wii golf, Gramophone, talon vesi, lamppuöljy. Thank you JMT (which buy the way is not so straight as it looks), thank you Otaniemi and all the people that I have met during these years.

Last but not least, I would like to thank my family of their endless support. Without you, my studies and this thesis would be just dream or perhaps not even that.

Teknikan kehdossa, 30.9.2019

Lauri Vähä-Savo

Contents

Symbols and abbreviations

Symbols

ϵ_r	Complex permittivity (ϵ'+$\hat{j}\epsilon$")
ϵ'	Real part of permittivity
ϵ"	Imaginary part of permittivity
ϵ_0	Permittivity of vacuum
μ_0	Permeability of vacuum
σ	Conductivity
Ω	Solid angle
G	Gain
$\hat{G}$	maximum gain that array can realize
$^\circ C$	Celsius degree
Γ	Reflection coefficient
τ	Transmission coefficient
λ	Wavelength
S_{xx}	Reflection coefficient of port x
S_{xy}	Isolation between ports x and y
w_n	weight of antenna port n

Operators

$[\cdot]^T$	Transpose
$[\cdot]^H$	Hermitian transpose (conjugate transpose)
$E[\cdot]$	Ensemble average
$\sum_{m=i}^{N}$	Sum from i to N
$\sqrt{\cdot}$	Square root
$\lvert\cdot\rvert$	Absolute value

Abbreviations

5G	Fifth generation mobile network
CA	Co-located array
CAD	Computer aided design
CDF	Cumulative distribution function
DA	Distributed array
Di	Deionized water
FDTD	Finite-difference time-domain
IE	Integral equation
IoT	Internet of things
PCB	Printed circuit board
PE	Polyethylene
TEM	Transverse electromagnetic
VNA	Vector network analyzer

1 Introduction

1.1 Motivation

Mobile phones have become one of most important communication devices that we use every day. The number of devices that are connected to the mobile network has increased rapidly all over the globe. At the same time, mobile phones have become much more than just a device that can be used for voice communication. The usage of mobile data has grown in Finland from 33 668 TB to 1 574 387 TB between 2010 and 2017 [1]. This means that every user in Finland uses almost 24 GB of mobile data every month. In Finland the growth has been quickest across the globe and hence Finnish users use most mobile date per registered sim card in the world [2]. The rapid growth of data usage has increased the interest towards millimeter wave frequency bands. When next generation mobile networks are to be brought into service, also new types of devices will be connected to network. Attaching new machinery, like security cameras, cars, hospitals equipment, home electronics etc., to the network is called internet of things (IoT) and it will take advantage of the upcoming fifth generation (5G) mobile networks. Adding a huge amount of new devices means that we will need more capacity compared to today's networks.

At the same time, in mobile devices, the size of screen and battery has been increasing, leaving less and less space for antennas in the mobile phone. Adding antennas also for higher frequency and having less space for antennas means that we need to be even more inventive when designing antennas for future mobile devices and evaluating performance.

The evaluation of antenna performance has evolved from basic free space evaluation, where interest is in characteristics like efficiency, realized gain, bandwidth and matching, towards much more complicated figures where the end-user and realistic environments are taken into account. This evaluation process is still ongoing and better ways to evaluate antennas are developed both in academia and industry. This thesis gives new insights into the characterization of antennas.

1.2 Scope and goal of the thesis

At the moment, there are no direct solutions or standards to evaluate antennas including the influence of the human body at millimeter waves. There are many different approaches to simulate the human influence on the radio channel, but there is only few studies that show measured radiation patterns over the solid angle for antennas under human influence [3], [4]. In this thesis the author will provide a literature survey of methods to evaluate antennas including spherical coverage and total array gain, different ways to mimic human and to analyze how a human is influencing the radiation of an antenna in mobile device. One of the scopes of this thesis is to find working solutions for considering the human body at 28 GHz over-the-air antenna measurements and in the end to manufacture an actual human phantom that can be used to experimentally evaluate antennas in a mobile device at millimeter-wave frequencies. The goal is to show the accuracy of the simulation

method so that it can be used for future work. To achieve the goal, two phased antenna arrays are designed, manufactured and measured, both in free space and with human phantom. Results from measurements and simulations are compared using spherical coverage.

1.3 Structure of the thesis

The structure of this thesis is as follows: Chapter two will introduce different types of antennas operating around 28 GHz and considers especially the electromagnetically coupled stacked patch antenna element. After considering a single element, the concept of phased antenna arrays and beamforming are discussed. Last, more comprehensive antenna evaluation methods are discussed. Figures of merits such as spherical coverage and total array gain are defined.

Chapter three surveys human tissue models used in previous works. After discussing human tissue's electrical properties, different types of human phantoms, designed for simulations and measurements, are introduced. In the end of chapter three, we review available methods to study the antenna-human interaction.

Chapter four discusses design and fabrication of human phantom for antenna measurements around 28 GHz. Human body scattering simulations are explained and differences between an accurate human model and a simplified phantom are discussed. After simulations, manufacturing process for the skin mimicking material is shown. Also permittivity measurement of the skin material are explained. In the end a mechanical design of the human phantom is shown and a phantom is manufactured.

Chapter five is describes the antenna measurements that were committed out. First the feed structures for antenna arrays are introduced and the fabrication of the PCBs is discussed. Next different types of measurements and measurement systems are introduced. The impedance matching and radiation patterns of the manufactured antenna arrays in free space are shown and discussed. Next the measurements with phantom is explained and results are compared between simulations and measurements. Finally, a beam synthesis is performed and the spherical coverage of measured arrays and simulated ones is calculated. Spherical coverage of manufactured arrays is compared to the simulated ones in free space and with manufactured human phantom.

Last chapter will conclude the work and give the key findings.

2 Measurements of mobile phone antennas at 28 GHz

2.1 Antenna elements for mobile phones at 28 GHz

In this chapter, electromagnetically coupled stacked patch antenna is introduced and used to build two different antenna arrays. 28 GHz is previously unused frequency range in mobile usage and multiple antenna designs have proposed for this region. Printed monopole, patch, slot and dipole antenna elements, both single and dual-polarized, have proposed for mobile usage [5] [6] [7]. In addition, combination of different types of antenna elements has been tested to get better coverage over the phone [8]. Figure 1 shows examples of these antenna elements. Increased size of battery and screen means that in the device we have less space to place the antennas.

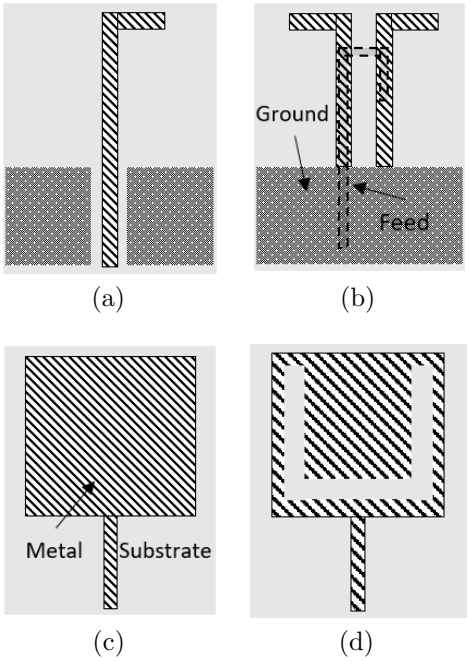

Figure 1: a) Monopole b) Dipole c) patch d) slot antenna element.

One promising antenna element design is electromagnetically coupled dual-polarized stacked patch antenna element due to its wide bandwidth. Increasing bandwidth means that more data can be send and received in the mobile. Figure 2 shows basic structure of stacked patch antenna. The lower patch is fed directly with coaxial or microstrip line via and the upper patch is parasitically fed from the lower patch. Introducing a small gap, filled with air or foam, between lower and upper substrate, can increase the bandwidth up to 20 % of center frequency [9]. In practice, manufacturing this air gap is hard at 28 GHz because placing patch elements by hand is near impossibility do to small tolerances. In PCB manufacturing process air gap is possible to do but the PCB might warp so much during the manufacturing that it does not stay in wanted tolerance range. There is also other problems with

manufacturing process, these are discussed at chapter 5.1. Without an air gap the stacked patch achieves usually ~ 8 % bandwidth [9]. In practice, upper, parasitic, patch is designed slightly smaller than the lower main patch. This way the resonant frequency of both patches are close to each other which results in a rather broad operational bandwidth.

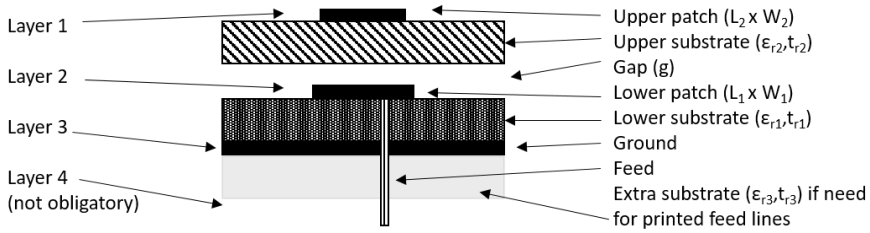

Figure 2: Basic structure of a stacked patch antenna.

The antenna element that we manufacture and use as the element in the evaluation in this work is presented in [10]. The element is an electromagnetically coupled dual-polarized stacked patch antenna, designed to resonate at 28 GHz with 3 GHz bandwidth at -6 dB matching level. Substrate is Rogers RO4450B that has relative permittivity $\epsilon_r = 3.52$. To achieve both polarizations, the element is fed from backside with two microvias whose diameter is 100 μm. Below the feed layer there is a ground layer. Between feed and ground layer is 101 μm substrate. After ground layer, antenna element has 101 μm substrate before lower patch. Feed vias goes through the ground layer. Between feeds and ground plane is 0.14 mm void so that feed via does not touch to the ground. Microvias are feeding lower patch at 175 μm from vertical and horizontal edge ensuring good isolation between both polarization. For horizontal polarization, the dominant component is θ, and of vertical polarization, it is the ϕ component. This is why these polarizations are also referred as θ and ϕ polarizations. Between parasitic patch and lower patch is 505 μm substrate. Antennas dimensions are illustrated in Figure 3.

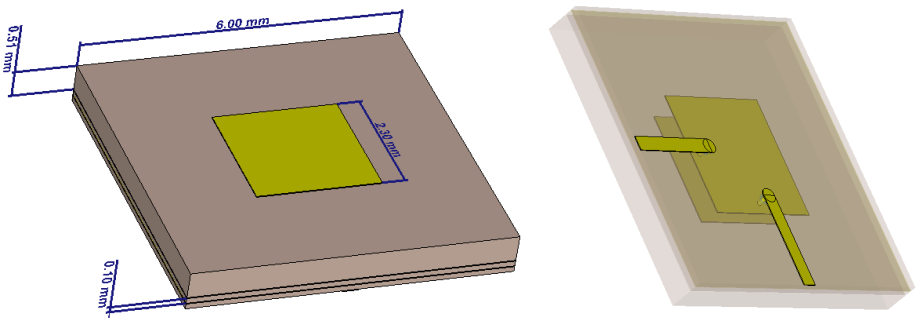

(a) (b)

Figure 3: a)Dimensions of designed antenna element, b) transparent illustration of the element structure from behind.

Matching and isolation of this single stacked patch element is shown in Figure 4. The element has 3 GHz and 2 GHz of bandwidth for -6 and -10 dB matching levels, respectively. The isolation between two polarization is better than -25 dB at -6 dB impedance bandwidth. The maximum gain is 5.95 dBi and radiation patterns are illustrated for $\phi = 0°$ and $\phi = 180°$ as well as $\phi = 90°$ and $\phi = 270°$ cuts in Figure 5. Figure 5a shows the element and feed points in spherical coordinate system. Red circle represents $\phi = 90°$ and $\phi = 270°$ cut and green circle for $\phi = 0°$ and $\phi = 180°$ cut. Cuts are almost same which is expected, because the patch is symmetrically squared.

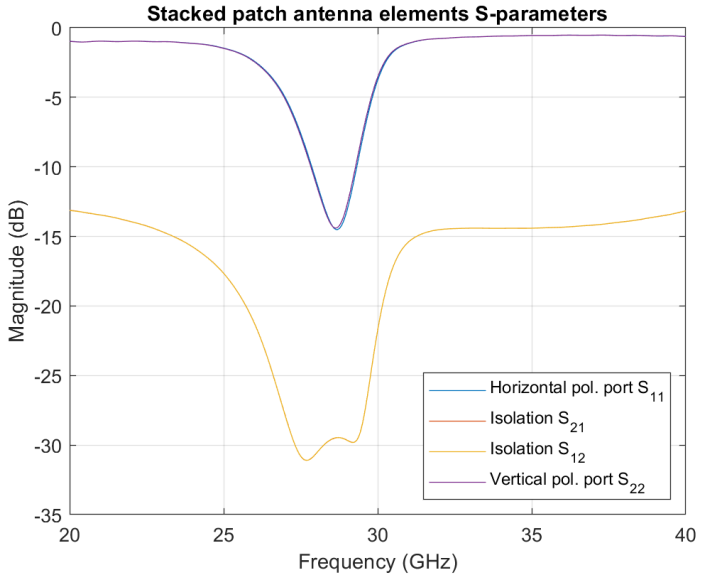

Figure 4: S-parameters of single stacked patch antenna element.

To provide realistic antenna systems for the antenna evaluation methods we propose and discuss in the later part of thesis, we designed and build from this antenna element two different antenna arrays, co-located array and distributed array. These two arrays can be seen in Figure 6. The co-located array has two, two-by-two, antenna modules located at the top left corner on the front side of a mobile phone and back side top right corner of backside. The distributed array has also two modules, but here all elements are individually located around both top corners so that all elements in one module are looking in different direction.

2.2 Antenna arrays for mobile phones at 28 GHz

In this chapter beam forming is introduced and different phase shifters are discussed. When we use high gain antennas to compensate increased path-loss, the beam-width of an antenna will get narrower and the area that a single antenna can cover will get smaller. To compensate smaller coverage we can use phased antenna arrays. The above introduced co-located and distributed arrays are both phased antenna arrays with sixteen feeds. Phased antenna array means that we can steer the beam

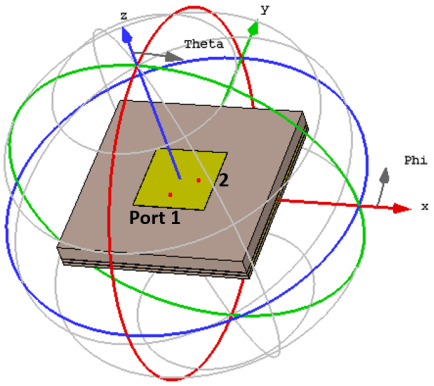

(a)

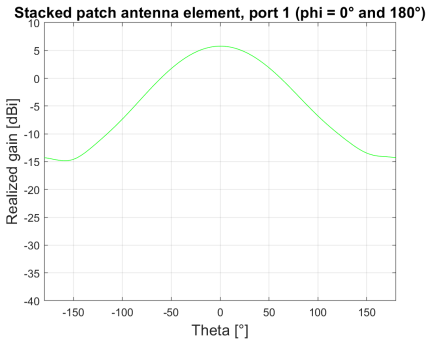

(b)

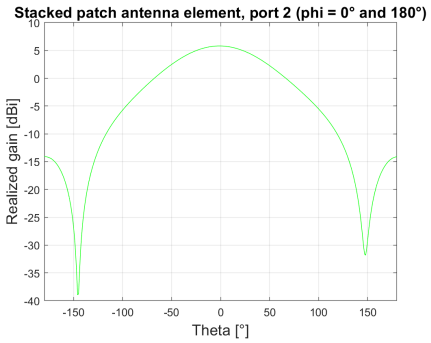

(c)

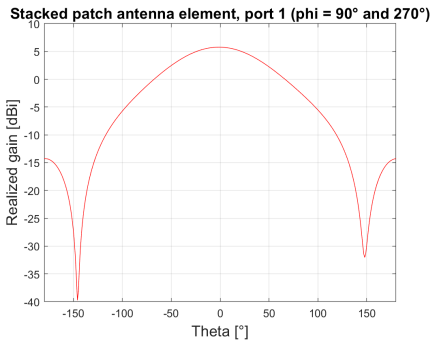

(d)

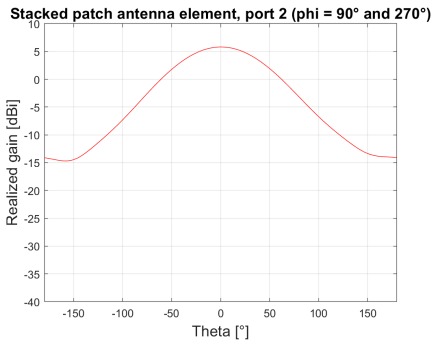

(e)

Figure 5: Radiation pattern of stacked patch antenna element a) antenna in the coordinate system including port numbers b) port 1 $\phi = 0°$ and $180°$ cut c) port 2 $\phi = 0°$ and $180°$ cut d) port 1 $\phi = 90°$ and $270°$ e) port 2 $\phi = 90°$ and $270°$.

electromagnetically by changing the phasing between all elements accordingly. Figure 7 illustrates a simple antenna array and the required manipulation of all sixteen received signals trough the sixteen ($N = 16$) weights. Each incoming signal (x_n) is multiplied with weight w_n^* to form the output signal y(t). w is n-length vector containing complex weights and $[.]^*$ is complex conjugate.

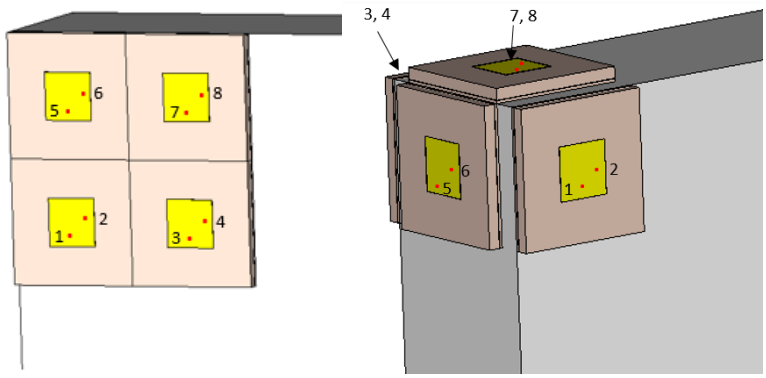

(a) (b)

Figure 6: a) Co-located array module, top-left corner on the front side of mobile phone (the second one on the backside of the top right corner not shown here), b) distributed array module (the second one on the top-right corner not shown here), left-top corner of mobile phone. All modules have eight feeds.

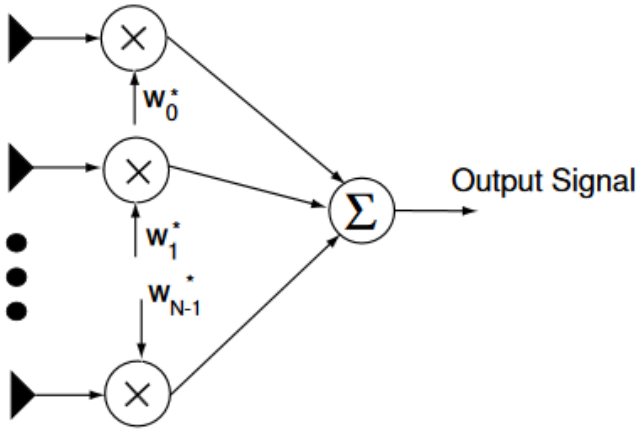

Figure 7: Example of weighted antenna configuration.

$$y(t) = \sum_{n=0}^{N-1} w_n^* x_n \tag{1}$$

$$= \mathbf{w}^H \mathbf{x} \tag{2}$$

The power of the array at any time is given by output signals magnitude squared so we can write output power as

$$P(t) = |y(t)|^2 \tag{3}$$

$$= \mathbf{w}^H \mathbf{x}(t) \mathbf{x}^H(t) \mathbf{w} \tag{4}$$

Where $.^H$ is Hermitian transpose.

In reality antenna signal phases can be manipulated with a device called a phase shifter. Phase shifters can for example use different length transmission lines as delay lines. This way we alter the propagation time and hence the phase of one of the N antenna feeds is turned [11, pp.534-535]. Another way is to introduce thin ferrite layer on top of a feed line. When part or all of microwave fields pass through the ferrite layer the phase velocity of signal is controlled by changing the permittivity of ferrite. Permittivity is controlled through a bias voltage or an external magnetic field across the ferrite. The ferrite phase shifters operate rather narrow but they are conveniently small in size [12]. In addition, MEMS based phase shifters have been used, but they are quite lossy and their power handling capability is usually quite low [13].

2.3 Figures-of-Merit

2.3.1 Spherical coverage

To be able to evaluate performance of phased antenna array it is insufficient to consider only peak gain, we also have to evaluate the total angular coverage of our array. Phased antenna arrays used in the mobile devices must be able to steer the beam to any direction to obtain best possible connection. Spherical coverage is obtained when we go through all possible phase combinations and corresponding beams and take the maximum gain at every angular direction (θ, ϕ) of the solid angle $\mathbf{\Omega}$ [14]. The maximum gain that an array can realize is defined by

$$\hat{G}(\mathbf{\Omega}) = \max_k G_k(\mathbf{\Omega}), \tag{5}$$

where $G_k(\mathbf{\Omega}) = ||\boldsymbol{g}_k(\mathbf{\Omega})||^2$ is the power gain of the k-th beam of an array, $\boldsymbol{g}_k(\mathbf{\Omega}) = [g_\theta(\mathbf{\Omega}) \quad g_\phi(\mathbf{\Omega})]$ is the complex gain vector including both polarizations; $\hat{G}$ can be characterised using its cumulative distribution function (CDF). The CDF gives us the probability to reach a certain gain, i.e. $CDF(x) = prob(\hat{G} < x)$, where $prob(\cdot)$ derives a probability of the condition specified in $(\cdot)$.

2.3.2 Total array gain

Another useful figure of merit is introduced by Haneda et al. in [15] and [16], where the novel evaluation method for phased antenna arrays in realistic double-directional radio channel environment is called total array gain (TAG). The total array gain is defined at the mobile station (MS) side as the ratio of power at the output port of the antenna array under test and the omni-directional dual-polarized antenna. At the base station (BS) side, the ideal isotropic dual-polarized antenna can be represented as $\mathbf{g}_{\text{omni}} = [1 \ 1]^{\text{T}} / \sqrt{2}$. Double-directional radio channel includes all L_p propagation paths between base and mobile station sides [17]. The double-directional radio channel can be calculated using ray-tracer [18], [19]. Ray-tracer provides multipath components seen from mobile station as parameters of multipath components $(\phi_l, \theta_l, \boldsymbol{\alpha_l}, \tau_l)_{l=1}^{L_p}$, where ϕ_l and θ_l represent angle of arrival of l-th multipath component, $\boldsymbol{\alpha_l}$ is polarimetric complex gain of l-th multipath

component, τ_l is time delay of l-th multipath component and L_p is total number of multipath components of the link. The received power in a mobile station can be expressed as

$$\tilde{P}_{\text{out}} = \left| \sum_{l=1}^{L_{\text{p}}} \boldsymbol{g}(\boldsymbol{\Omega}_l) \boldsymbol{\alpha}_l \boldsymbol{g}_{\text{omni}} \right|^2 . \tag{6}$$

Because the instantaneous power is affected by small-scale fading, we average them out over sample realizations of $\boldsymbol{\alpha}$ for each multipath components to get estimation of mean power, $P_{\text{out}} = E_{\boldsymbol{\alpha}}[\tilde{P}_{\text{out}}]$. $E_{\boldsymbol{\alpha}}[\cdot]$ is the Ensemble average over small-scale realization $[\cdot]$. Random phase over $[0, 2\pi)$ is introduced to the realizations of $\boldsymbol{\alpha}$ while keeping magnitude constant. Total array gain is finally derived as $G_a = 10\log_{10}(P_{\text{out}}/P_0)$ where $P_{\text{o}} = E_{\alpha}[\tilde{P}_{\text{o}}]$ is the omni-directional mean link gain and $\tilde{P}_{\text{o}}$ is received power at mobile location

$$\tilde{P}_{\text{o}} = \left| \sum_{l=1}^{L_{\text{p}}} \boldsymbol{g}_{\text{omni}}^{\text{T}} \boldsymbol{\alpha}_l \boldsymbol{g}_{\text{omni}} \right|^2 . \tag{7}$$

The total array gain is visualized through its CDF. Total array gain combines the gains of the whole array, as well as the gains to signal precoding or combining. The main difference to the conventional array gain is that total array gain is defined uniquely. The array gain depends on the element that is chosen from array as reference. Received power of a single antenna array element can vary heavily depending on its polarization, orientation and type in an operational multipath environment. With total array gain, we can unambiguously compare different realizations of phased antenna arrays in a realistic multipath propagation environment.

3 User effects on mobile phone antenna performance

3.1 Human body effect

Shadowing effects of the human body on electromagnetic radiation at high frequencies is well known, but phantoms for measurements are not common. In some papers, methods based on calculations use knife-edge model for the human, and in measurements real human is used [20],[21],[22]. Although an absorbing knife-edge mimics human quite well, we cannot compare these results to measurements with actual humans and expect that they are similar. Simplified human models have been used in simulations. For example [23] has used a rough model for a human inside a huge stadium simulation. The authors used three square blocks to model humans in the performance evaluation of millimeter wave cellular networks. Many papers also consider only the effect of the finger on the antenna [24], [25]. This approach does not reveal the shadowing of other parts of the human holding the device. In [4], authors performed measurements at 60 GHz with salt-water filled cylinders that mimic the legs of human. They also used human head and upper torso phantom that were filled with salt water. This approach gave similar results as simulations with human model but a full sized phantom of this type would be too heavy and hard to use in full-3D pattern measurements of antennas. There are also commercial phantoms, manufactured for example by Speag. These manufacturers have different body parts for low (0.3-3 GHz) and for high frequencies (up to 110 GHz). The phantoms are accurate hand and head models, that have been used in radiation pattern measurements [26]. One problem with these commercial phantoms is that getting a full human phantom is expensive and more importantly that we have no control over the phantoms performance. Many times, both at low and high frequencies, real humans have been used in radiation pattern measurements. This approach has problems with repeatability of the measurement. Repeating the same measurement is nearly impossible.

Recent studies have used accurate human body models in simulations. An accurate CAD model of a human is shown in [27]. This model is made using "make human" software that can be used to create accurate human model with various body dimensions. The model used in [27] is a male with 170 cm height that consists of over 14000 polygons. This model is coated with a material that has same electrical properties as Gabriel's skin characterization. In this thesis, we use this human model as reference human model.

3.2 Antenna-human interaction

The far field shadowing effect of humans has been shown to have significant effect on the propagation channel. If there is an object in the vicinity of the antenna, then the antenna resonance can detune and radiation efficiency can decrease. This applies for example to the fingers, arm and palm of the user. This detuning of finger on the mobile antennas has been studied around 1 GHz in [28], at 60 GHz in [24] and

at 28 GHz in [25]. These papers consider effects of a finger to the radiation but omit rest of the full human study out. Because a user is close to the antennas of the mobile phone, we must consider effects of the user also in term of detuning and not only in terms of shadowing. Some simulation studies have been made with full human models [27] and some phantom measurements were performed in [4], but measurements with a human phantom across the whole solid angle have not yet been done at 28 GHz. Zhang et al. carried out a user effect analysis at 28 GHz in [3]. The study performed a thorough simulation based analysis of the antenna performance at 28 GHz, but in measurements they used actual humans for full-3D pattern measurements. The repeatability of measurements is important and a using living human increases error as human will move during measurements.

As can be seen, there are only a few studies considering the human effect near the antenna and most of those studies are simulation studies. Measurements are performed with living human and hence subject to uncertainty. Radiation pattern measurement covering the entire solid angel for antenna elements under influence of a human body in a repeatable manner at 28 GHz have not been done. This work tries to fill this gap by realizing repeatable measurements including human phantom.

3.3 Electrical properties of materials

Materials can be roughly divided into two classes, conductors and dielectrics (also called insulators). Most material are dielectrics and this chapter will consider these. When an electric field is introduced to a dielectric material, electric charges will not flow as they do in conductors but only slightly shift from their original position causing dielectric polarization [29]. A material's electrical properties dependent on its dielectric properties. Accurate measurements of dielectric properties are necessary when designing materials. A material is dielectric if it is able to store energy. Permittivity, permeability and resistivity are called dielectric properties. Because human tissues are not magnetic, we do not need to consider permeability here. Permittivity is a complex quantity $\epsilon^* = \epsilon' - j\epsilon''$ and it is frequency dependent. The real part of permittivity, ϵ', describes the ability to store energy in the material. The imaginary part, ϵ'', describes losses in the material. The imaginary part is always greater than zero and it represents dielectric and conductive loss. Often these are referred as relative permittivity (ϵ') and conductivity (σ). Imaginary part of permittivity and conductivity are related to each other by angular frequency, $\sigma = \omega \cdot \epsilon''$. In this work, we use complex permittivity instead of conductivity. The permittivity is quantified by $\tan\delta$, which is also known as loss tangent or tangent delta. The loss tangent represents the ratio of the imaginary part to the real part of complex permittivity, i.e. the ratio of lost energy and stored energy.

3.4 Human tissue models

The interest in the electrical properties of human tissues has grown during the past 25 years. Especially using micro- and millimeter waves in medical applications has driven research. S. Gabriel released his research of dielectric properties of human tissues

in 1996 [30]. In his research, he measured relative permittivity and conductivity of a huge amount of different human tissues. After measuring, Gabriel and his team applied Cole-Cole fit for all the measured tissues. They released these Cole - Cole parameters from 10 Hz up to 100 GHz. Alekseev made simular measurement for human skin and his measurement results agreed with Gabriel's results [31].

Especially skin, fat and muscle tissue models at micro- and millimeter waves have been studied a lot. These tissue models have been used for example to develop methods to detect breast cancer using microwaves [32], [33]. For our study, the main interest is in skin equivalent materials because the penetration depth of electromagnetic waves in skin is only 0.92-0.95 mm at 28 GHz according to Gabriel's study. Skin can be considered as three-layer material composed from epidermis, dermis and fat layers. The thickens of the human epidermis and the dermis varies in the range of 0.06–0.1 mm and 1.2–2.8 mm [34]. Therefore, the electromagnetic waves do not penetrate further than into the skin.

For mimicking human skin, two different skin phantom models have been reported and widely used. These models are gelatin-based and polyethylene-powder-based models. Both gelatin- and polyethylene-based models contain approximately 65 % of water, which is the same amount as human skin [35]. Gelatin is made mostly from pigs skin so it contains similar proteins and carbohydrates as human skin. Therefore, a gelatin-based phantom models skin rather well. The easiest way to manufacture skin phantom is using gelatin as [36], which shows that the phantom can be made from three ingredients, deionized water, agar and gelatin. Gelatin has one unfavorable property; it is organic material and can rot. The phantom shown in [37] is polyethylene-based. This model was originally designed for 57–64 GHz range but in [38] this model was measured below 50 GHz and works well also at 28 GHz. Polyethylene is plastic so it does not change over time. This phantom has also a bit of biological material agar, but its amount is ~ 2 % in the solution. This phantom is discussed more in chapter 4.

4 Design and fabrication of a human phantom

4.1 Design

To be able to perform measurements including human body, one needs a phantom that mimics the human well enough at the wanted frequency range. This phantom needs to be made from a material that has similar reflection properties as human tissue and the shape of human. Figure 8a show a highly accurate human model which was showed in [27] and discussed in chapter 3.1. Manufacturing of the accurate human would be challenging and we decided to design a simplified human phantom. The simplified phantom should have roughly same dimensions as the accurate human model but shapes will be simplified. The simplified phantom is made up of four parts; hand palm, arm, torso and head. Head and torso are made as two cylindrical pieces, arm and palm are made from two square pieces. The simplified phantom is illustrated in Figure 8b. To be sure that reflection properties of this simplified phantom is close to the accurate human model we will compare them terms of radiation pattern and spherical coverage in simulations. The comparison is done in next section. As mentioned in chapter 3.1 weight of the phantom needs to be as low as possible. Because we need to mimic only human skin, inside of phantom should be some light material. Good material for frame of phantom is Styrofoam as it is light, unyielding and is relatively easy to shape. To help joint pieces to each other is wooden pole in the middle of torso and head. Piece of plywood is added at the bottom end of torso to the wooden pole to help attaching phantom to our anechoic chamber. Section 4.3 will describe manufacturing process of the phantom in detail.

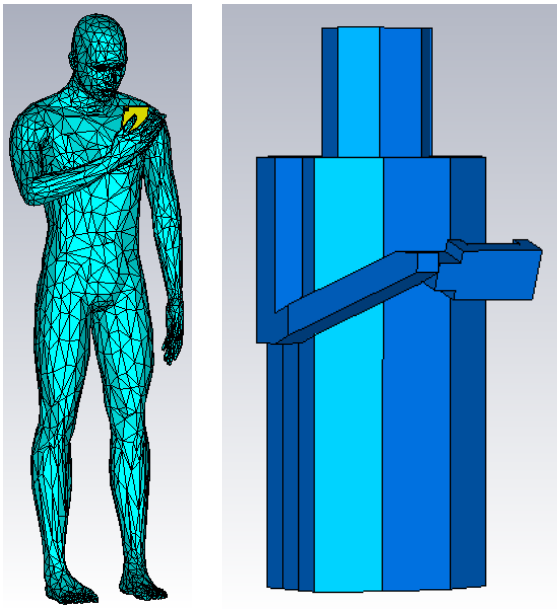

(a) (b)

Figure 8: Illustration of a) a simplified human phantom intended for measurements b) a highly accurate human model for reference simulations.

4.1.1 Verification of the hand palm

For this work, we decided to manufacture a simple hand palm that would still affect in the antenna arrays same way as a real human palm. The palm is a rectangular box with immersion for antenna arrays. Using the simple shapes, we can manufacture the exact shape as we have designed and used in simulations. Antenna arrays are placed in middle of the palm. Figure 9 shows simulated azimuth cut of the realized gain with accurate hand and simplified hand holding the co-located and the distributed arrays. Azimuth cut is on plane of $\theta = 90°$ and elevation cut is a plane of $\phi = 90$ and 270°. In Figure 9c and d azimuth and elevation cuts are the blue and red circles, respectively. Feed 1 represents characteristics of most ports and feeds 5 and 13 show biggest difference between original and simplified phantom palm. As we can see, difference in realized gain between original and simplified palm is small for all antenna elements. Average difference for azimuth and elevation cuts for the co-located array is between $0.12 - 0.93$ dB and for the distributed array difference is between $0.19 - 0.85$ dB. The small difference tells that hand is far enough from antennas so that possible de-tuning effect is minimal.

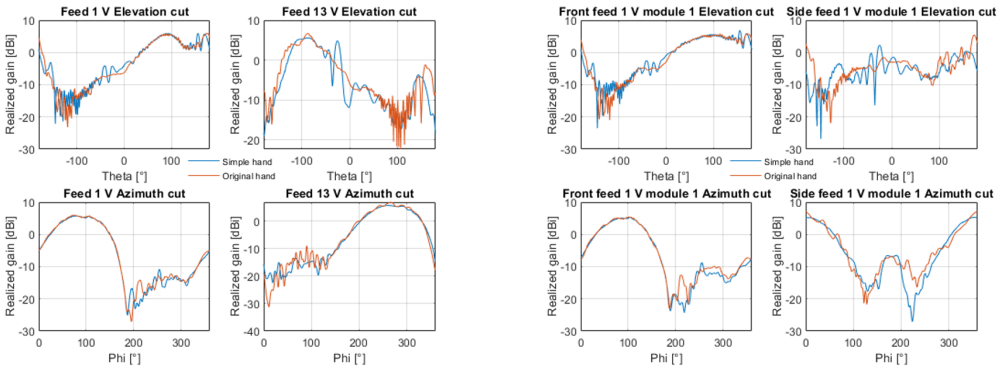

(a) (b)

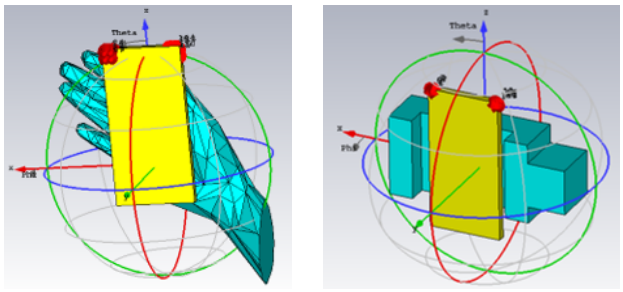

(c) (d)

Figure 9: a) Realized gain of the co-located arrays with an accurate and the simplified hand palm. Elevation and azimuth cuts of ports 1 and 13. b) Realized gain of the distributed arrays with an accurate and the simplified hand palm. Elevation and azimuth cuts of ports 1 and 5. c) Orientation of an accurate palm in simulations and d) orientation of the simplified palm in simulations

4.1.2 Verification of the phantom

In this section, the reflection properties of the simplified phantom are compared to ones of the accurate human model. It is not feasible to perform full phantom simulations with FDTD because the phantom is too big. Simplified phantom does not have legs but its height is still 86 λ at 28 GHz. If we would use FDTD to simulate this situation the number of meshcells would be around 1.5×10^9 which means that needed calculation power and time will be too high with full sized human model. To avoid this problem we took an approach shown in [10] and [27] to make simulation faster without losing accuracy. This simulation model uses the integral equation (IE) solver instead of FDTD solver. We insert field sources of antenna arrays, which we simulated with the hand palm, over the hand palm and the mobile phone chassis. It is important to leave the palm and the mobile phone chassis inside of filed source to ensure possible blockage of the radiated field. The surface of phantom is simulated as lossy metal covered with skin layer. There is no actual skin layer in the simulation but the surface impedance of the phantom is same as human skins. Using this kind of method, we can do simulations with full sized phantom in a few hours.

To be sure that we have thick enough skin layer in simulation, we did two different checks. First, we made sure that surface impedance is converged to a constant value and it does not change if we increase the layers thickness. Second, we checked that reflection coefficient has also converged to a single value. Behavior of reflection coefficients of the skin over different thickness is shown in Figure 10. Reflection coefficients of skin with changing thickness was also calculated using a method described in ITU-R Recommendation P.2040-1 [39] in addition to CST simulations. After thickness of 1.5 mm the reflection coefficient of skin changes only marginally. 1.5 mm is also thickness of human skin in reality.

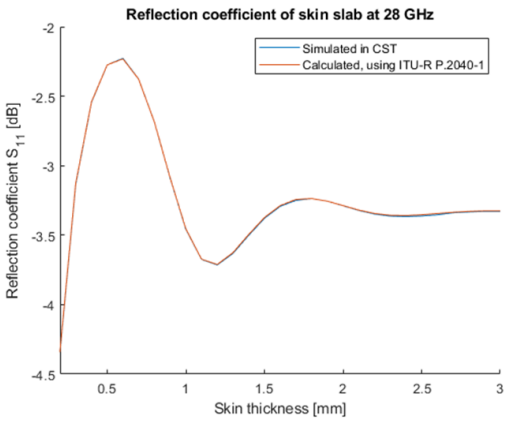

Figure 10: Reflection coefficient of skin, simulated and calculated.

After full phantom simulations are done, we need to compare radiated field of the antenna arrays with simplified phantom to accurate human model. We use the same method that is shown in [10] to calculate the maximum realized gain and spherical

coverage. We use ideal three-bit phase shifters to synthesize 512 different beams for both co-located and distributed array. When we have calculated maximum gain of all possible beams we need to reposition calculated realized gain uniformly to the sphere. When we measure or simulate antenna array we get electric field at every certain interval of θ and ϕ angles. This way we have more points on the poles than on the equator of the measured sphere and it will affect spherical coverage. To equalize the density of measurement angle across the solid angle we need to interpolate new data set that is distributed with equal density [40]. These points can be calculated by inserting spiral inside of sphere so it starts from pole and goes against surface of sphere to other pole and calculating points on this spiral [41]. Figure 11 has sphere with the spiral and 101 equally dense points for demonstration. From this uniformly

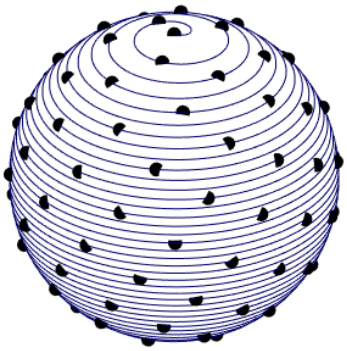

Figure 11: Sphere and spiral visualizing the procedure to create to calculate equally dense points.

dense maximum of realized gain, we can calculate CDF of spherical coverage and compare easily differences of the realized gain between an accurate human model and the simplified human phantom. Figures 12 and 13 shows maximum of realized gain of the co-located and the distributed array in 2D plots. From 2D plots it can be seen that, especially with the co-located array, phantom's flat surfaces direct radiation differently compared to an accurate human model. The smooth surfaces of the simplified phantom reflect radiation where accurate human model scatters it more broadly to different angles. In the distributed array plot a difference is not so big but some differences can be seen especially around area that the arm is shadowing. Because the arm is squared shaped, it creates bigger shadow than accurate human arm. This is highlighted with the distributed array that has an antenna element on the side of a phone chassis.

Figure 14 shows CDF of spherical coverage for both co-located and distributed arrays. CDF of spherical coverage with the simplified phantom start to differ under 0.4 probability level from the accurate human model and difference is 2 dB at 0.1 probability level. The Distributed array with simplified phantom gets peak gain 0.6

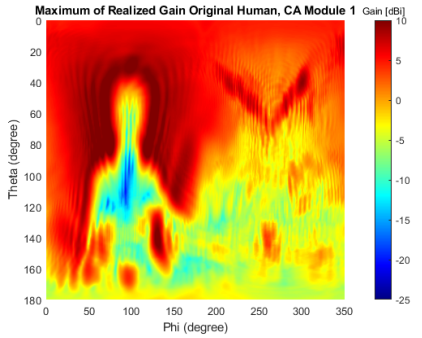

(a) CA module 1 accurate human

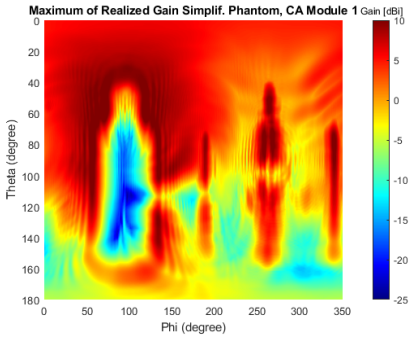

(b) CA module 1 simplified phantom

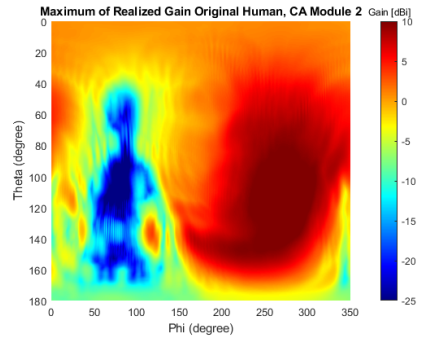

(c) CA module 2 accurate human

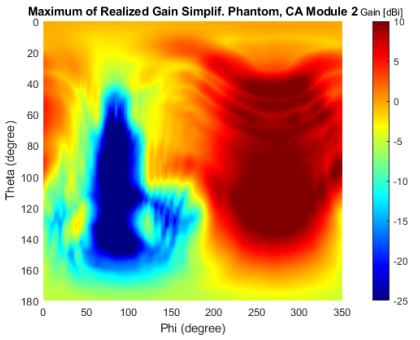

(d) CA module 2 simplified phantom

Figure 12: 2D plot of spherical coverage of co-located array with both original and phantom.

dB higher than the accurate human model but after 0.4 level it starts to get lower values and at 0.1 probability level difference is 3.7 dB. Overall it can be said that this simplified phantom models human well and we can use it in measurements.

4.2 Skin material and fabrication

4.2.1 Skin material

In the literature, we can find two widely-used materials that mimic human skin in broad frequency band and manufacturing is easy, fast and inexpensive. These materials are gelatin based model [32] and polyethylene (PE) powder based models [37][38]. For this thesis, we decided to work with polyethylene-based model because it is faster to make than gelatin-based model, a gelatin model takes 5-7 days to be ready. Moreover polyethylene-based model has less biological material that could decay. Chahat et al. designed skin material from deionized water, agar, TX-151 and polyethylene powder at 60 GHz [37]. Dancila at al. showed at [38] that the same material mimics skin well also in lower and higher frequencies.

Human skin is mostly water ($\sim$ 65 %) [35] and hence the base of these materials is also deionized water which mostly determine dispersive properties of the material. Waters permittivity is higher than skins so we need to add some material that has

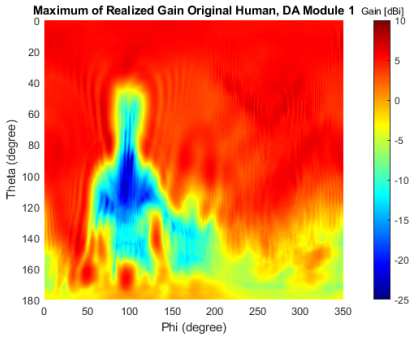

(a) DA module 1 accurate human

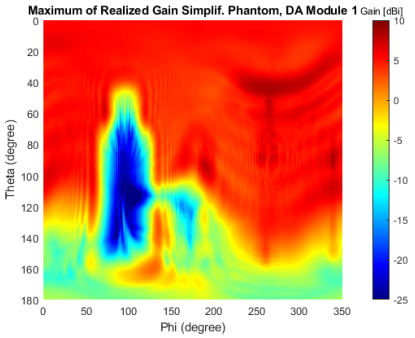

(b) DA module 1 simplified phantom

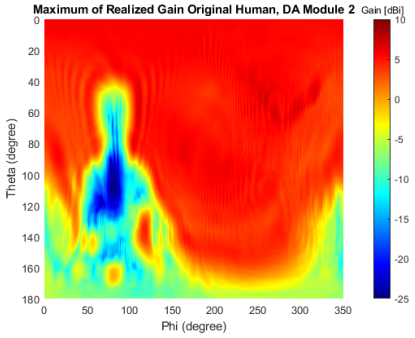

(c) DA module 2 accurate human

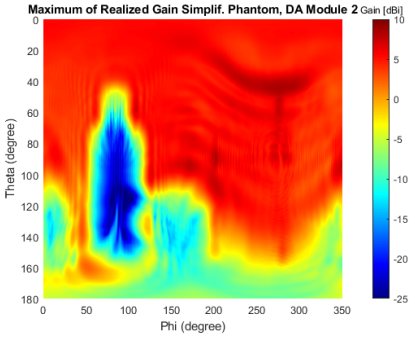

(d) DA module 2 simplified phantom

Figure 13: 2D plot of spherical coverage of distributed array with both accurate human model and simplified phantom.

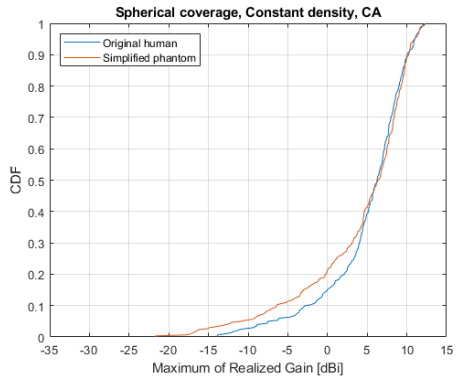

(a) The co-located array

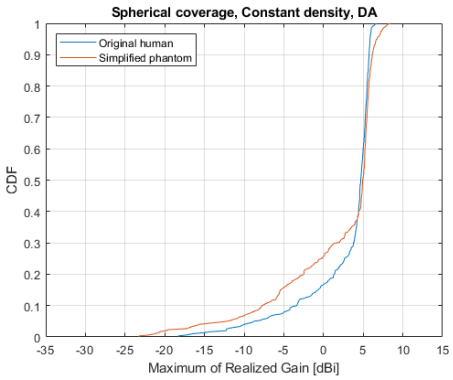

(b) The distributed array

Figure 14: Comparison between the spherical coverage CDF of original human model and simplified phantom spherical coverage CDF.

lower and steady permittivity over large frequency range. Water's permittivity is tuned with polyethylene powder to match it with skin. The real part of permittivity of high-density polyethylene is 2.35 and imaginary part is around 10^{-4} over wide frequency band [42]. Steady permittivity of polyethylene makes it easier to predict

materials permittivity, when it is mixed with different amounts of water. In this work we used high-density polyethylene but one can use also low-density polyethylene as its permittivity has 0.05 difference to high-density polyethylene [42]. We used HE 2550 polyethylene manufactured by Borealis AG. Granule size of HE 2550 is unknown and effect of granule size to complex permittivity was not investigated during this work.

Agar is introduced to water to make model semi-solid. Agar is mixture of two components, agarose and agaropectin, and it is collected from certain red-purple algae. Agar is widely used in food industry as vegetarian option for gelatin. Agar is used in this application for its retention of self-shaping. Agar makes solidifies water solution at 1-2 % when it is at room temperature [43]. Chahat also says in [37] that agar in small quantities (< 4 %) does not affect to electrical properties of material. This means that we can tune solidity of the material quite freely for different applications easily. Chahat mentions that agar and polyethylene do not mix with each other directly so we need to use TX-151 to increase viscosity of solution. TX-151 designed and mainly used to change, control or vary the properties of water. TX-151 reacts with water and end product varies from high lubricity liquid to stretchable rubbery material [44]. TX-151 can be added either cold or hot water. If TX-151 is added to hot water it may lump, but lumps should disappear the next day. TX-151 also increases elasticity of material. In addition, one can use sodium azide as preservative but it does not affect electrical properties. Sodium azide is harmful for living tissue and works well as preservative. For this project, we decided to leave it off. Chahat gives amounts of ingredients that they have used but while testing we noticed that material is too soft for our application. We doubled amount of agar from 1.5 g to 3.0 g to get harder material. Also other ingredient quantities were tuned to work better for our use. Used solution is shown in Table 1

Ingredients	Mass (g)
Deionized water	100
Agar	3
TX-151	4
Polyethylene powder	36

Table 1: Materials and amounts used for material mimicking human skin

4.2.2 Manufacturing skin material

In this chapter, the practical implementation of the skin material designed in previous chapter is discussed in detail. First deionized water at room temperature is measured to a container. The agar is added to water while water is stirred until agar is dissolved in to water. It is important that the agar does not agglomerate and the solution stays homogeneous during the whole process. After all agar is fully dissolved in the water, TX-151 is added to the solution. Also while adding the TX-151 powder,

the solution needs to be stirred. TX-151 is added in small quantities while stirring the solution to avoid lumps. Very small lumps of TX-151 do not pose a problem because such small lumps will disappear during the cooling down of material. As a next step, the temperature of the solution is increased up to 80 °C. Thereby, the solution will pasteurize when its temperature is at least $\sim$ 75°C for at least 30 seconds. Pasteurization will make sure the material usable for many month. The solution still needs to be stirred during heating to avoid hot spots. When the solution is at 80 °C polyethylene powder is added. Polyethylene can be added in small amounts to make mixing easier. It is important to remember that the final solution needs to be homogeneous; polyethylene must be distributed uniformly in the material. The temperature needs to be between 75 and 90°C to keep solution in a liquid form while it is prepared. After the solution is mixed, it can be poured to a mold to cool down. The material needs to cool down to room temperature to become semisolid and be ready for use. Agar needs $\sim$ 16 hours to bind all the water and make the material hard. Covering the material during the cooling down prevents water from evaporating and ensures the wanted dielectric properties. Skin material manufacturing instructions with pictures can be found in Appendix A.

4.2.3 Permittivity measurements of the skin material

In this section, the material properties of the skin material are confirmed. One way to measure permittivity is to measure the reflection coefficient of a material for an incident electromagnetic wave and calculate the permittivity from the reflection coefficient. For this thesis, the dielectric measurements were performed with an HP 8720c VNA and HP 85070a dielectric probe kit. The measurement probe is connected to the VNA with coaxial cable. The VNA is connected to a measurement PC with HP-measurement software. The software acquires all measurement data and calculates the complex permittivity. The exact operation of the software is not documented, but authors in [45] say that it is most likely as shown in [46]. Our setup can measure across a frequency range from 50 MHz up to 20 GHz. The measurement probe is an open-ended coaxial probe. It can be used for liquids and semi-solid materials. Calibration is performed by measuring three known materials mainly 1) air, 2) metal (short), and 3) deionized water. During the measurement, we ensure that the probe at all times the probe touches the material and there is no air bubbles between the probe and the material under test to ensure accurate permittivity estimate. Part of the RF signal exiting from the probe enters the material under test, while part of it is reflected back into the probe. The reflected field is measured and related to permittivity. The material under test should be at least $20/\sqrt{|\epsilon_r'|}$ mm thick to be allow neglecting the effect of multiple reflections inside the material under test. Figure 15 shows our measurement setup. The operation of the measurement setup is described in detail in [45].

To make sure, that our material mimic's skin well, test pieces containing 90 %, 80 % and 70 % of water were manufactured and the permittivity of these test pieces was measured. Real and imaginary parts of the permittivity are shown in Figure 16. Increasing the amount of polyethylene powder decreases both real and imaginary

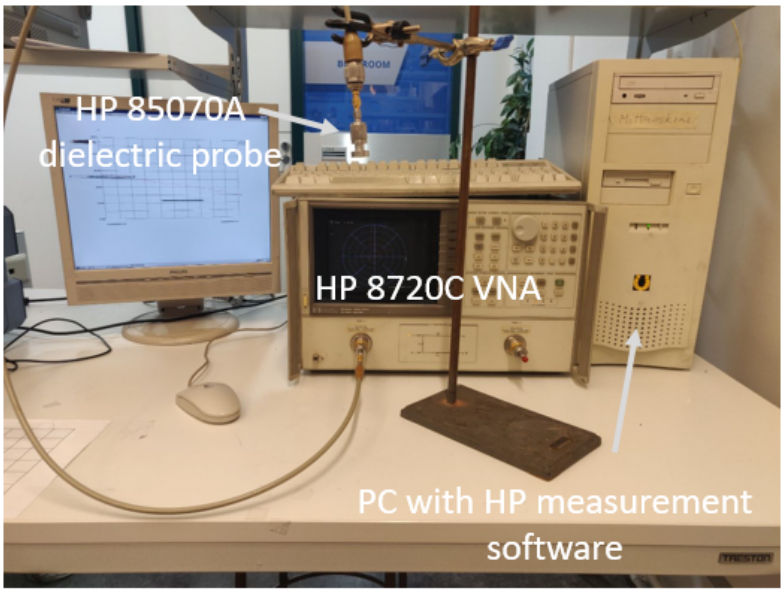

Figure 15: Permittivity measurement setup.

part of the permittivity. We can tune the amount of water and polyethylene powder so that the permittivity aligns with Gabriel et al. [30] permittivity model.

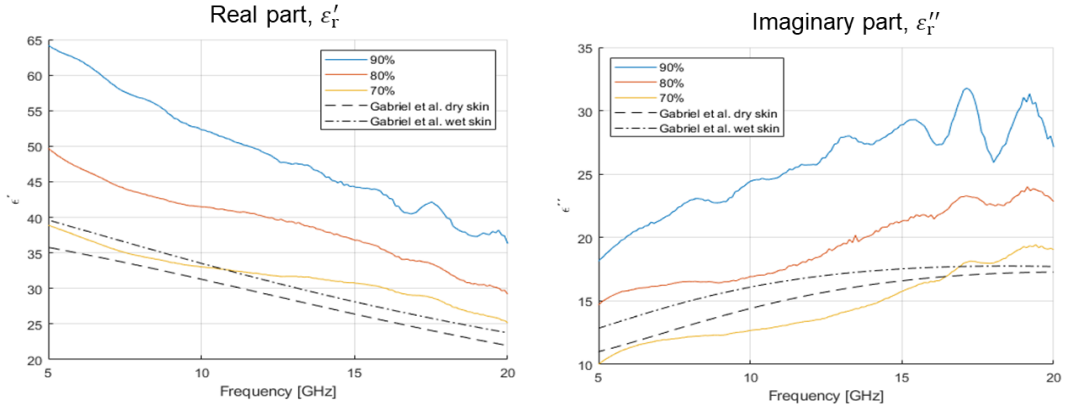

(a) (b)

Figure 16: Comparison of permittivities for material test pieces containing 70 %, 80 % and 90 % of water, a) real part of permittivity b) imaginary part of permittivity.

We noticed that water evaporates from the material, which caused the surface to harden and the electrical properties to change significantly. To prevent water from evaporating, a thin plastic film was introduced on top of the skin material. Possible effects of this thin film on reflection coefficients of our material are studied. The use of open-ended coaxial probe was not suitable in this case because good connection between the probe and the material covered with a plastic film could not be achieved. We instead measure the reflection coefficients horn antenna to determine the reflected

power from the material surface including the plastic film. It is important that the distance between antenna and material does not change during the measurement. Changing distance will change free space path loss and measured reflection will be different. Like in permittivity measurements, it is important that cables and antenna do not move after the calibration of VNA to prevent changing of phase and reflection. The fabricated skin material was measured without any film, one and two layers of plastic film on top of it. The frequency range of the measurement was from 26.5 to 30 GHz with 1601 measurement points. The distance between antenna aperture and the fabricated skin material was 22 cm.

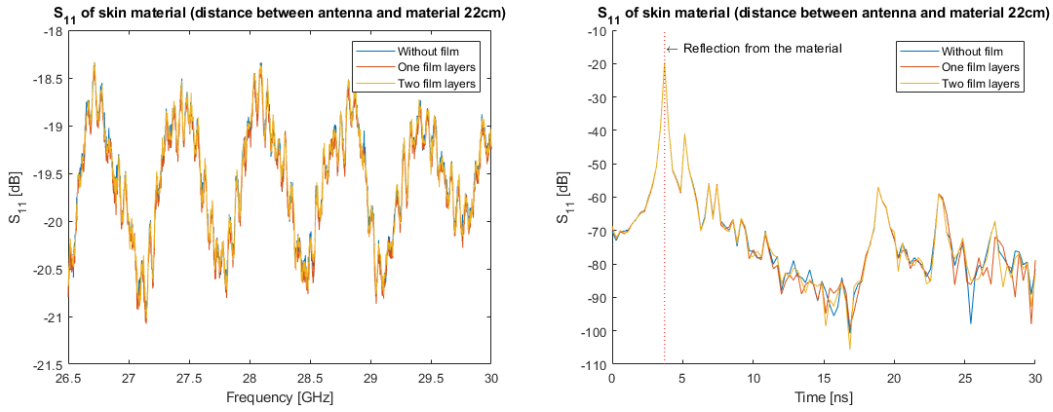

(a) (b)

Figure 17: Reflection coefficient of skin material with two, one and without plastic film in a) frequency - and b) time domain.

The reflection coefficient for all three cases, shown in Figure 17, align almost perfectly, which means that film has no effect reflection coefficient and this is good solution to prevent evaporation of water from material. In Figure 17b a spike at 3.7 ns is reflection from material and later ones are either multiple reflections from material or the unwanted reflections from the laboratory environment. The unwanted reflections cause oscillation seen in Figure 17a. Maximum differences between measurements is 0.13 dB. The reflection coefficient of thin plastic film was also calculated using method described in [47] chapter 3. Thin plastic film is low-density polyethylene and real and imaginary parts of the permittivity are 2.3 and 10^{-4}, respectively, according [42]. Reflection coefficient of 0.1 mm film was estimated to be -28.4 dB at 28 GHz, which indicated also that film has no effect to the reflection coefficient of material.

We made permittivity measurements for the same 70 % material that was made at the beginning of this work. The skin material sample was kept in plastic bag between measurements to ensure that water cannot evaporate from the material. In Figure 18 shows the permittivity of the skin material over four month. The permittivity does not change during three months. After four months of manufacturing the skin material, there is clear change in the permittivity. The agar is probably starting to decay and a part of water is lost from the material. This indicates that the skin

material can be used three months after it has been manufactured.

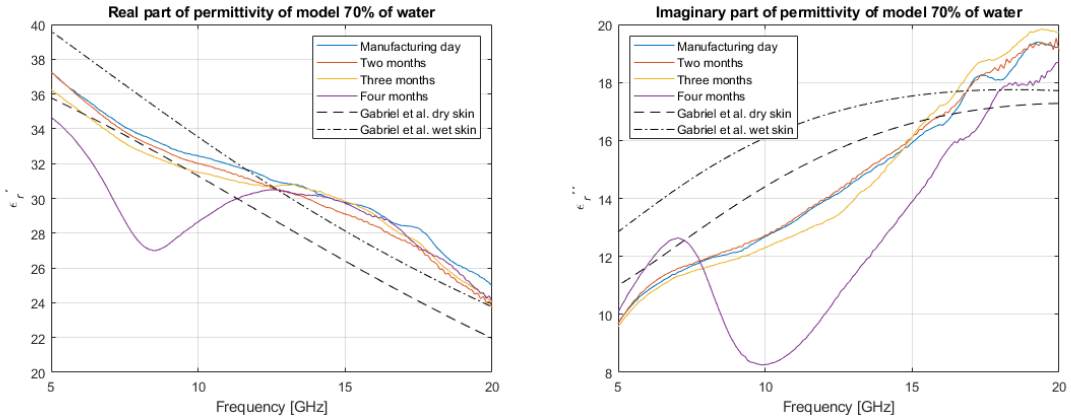

(a) (b)

Figure 18: The permittivity of the skin material over four months time a) real and b) imaginary part of permittivity.

We made thin plates of skin material that can be placed on top of the phantom using a plastic film. The phantom has approximately 1.2 m^2 surface and thickness of skin was decided to be 5 mm. According Figure 10 we could use thinner layer but to ensure the handling of the plates was the thickness increased. This means that skin material for whole phantom will weight roughly 6 kg. Increasing thickness of the skin material by 1 mm means approximately 1.1 kg increase to the total weight. It is important to know the weight of the model as we need to mount it on a rotator in the anechoic chamber. In our case the limit of the rotator is around 13 kg.

4.3 Manufacturing the phantom

Styrofoam was chosen for a base material of the phantom. It is closed-cell extruded polystyrene foam board that is usually used as thermal insulator. It is hard and does not bend or break easily but is still light. All these properties are good for the base material of the phantom. The phantom's dimensions can be seen from Figure 19a and the structure of the phantom torso and head is illustrated in Figure 19b.

First, we cut Styrofoam to right width and height. For torso we need two 100 mm and one 50 mm thick pieces which are 329 mm wide and 710 mm long. 100 mm pieces are outer parts of torso and 50 mm is a center piece. From the 100 mm thick boards two corners are cut away so that 50 mm from thickness and 100 mm from width is cut with hot wire. 50 mm center piece is cut in two so that 50×50 mm wood pole can be fitted to middle of phantom. Next we need to make immersion from plywood to the bottom side of the torso. To the plywood we attached threads which help attaching phantom to the measurement tower in the chamber. After all this is done, we can glue parts together. We used strong assembly mastic to glue parts to each other. It is important to check that pieces are level in each other at sides. Plywood can be attached at this point. Three screws are embedded to the

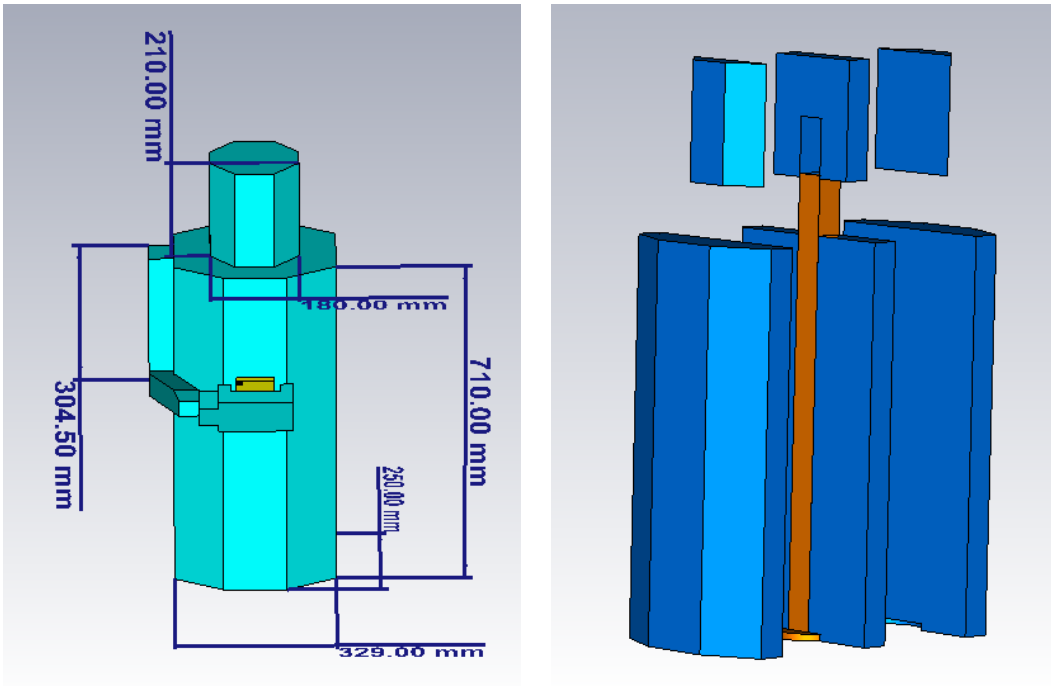

(a) (b)

Figure 19: a) Dimensions of the designed phantom b) Structure of designed phantoms torso and head.

wooden pole to ensure durability of the plywood. It is good to put also glue between Styrofoam and plywood. While torso is drying, pieces for head can be cut. Head is made of three 50 mm thick Styrofoam pieces that are 180 mm wide and 210 mm long. Outer corners are cut so that 50 mm from thickness and width is cut away. To center piece of the head we make a hole for wood pole. The hole is not going all the way through but only to half way. The hole needs to be tight to fit the pole to ensure that head does not fall of during measurements. Head is not glued to the wooden pole, this makes easier to place skin material on top of phantom. After all pieces for head are ready, we can glue them together. Next, we need to make arm. Arm has lot of shapes and it is made out of one piece of Styrofoam to ensure physical endurance. Arm is made from one 100 mm thick Styrofoam and cut with hot wire and band saw. First, we need to draw silhouette of arm to the Styrofoam and cut the basic shape of the arm. Next, we start to cut arm closer to right shape side by side. It is good to check dimensions after every cut. It is important to get arm as close to original model as possible to ensure minimum error in measurements. Last part is to make a hand palm by cutting Styrofoam with hot wire and band saw. Finished phantoms dimensions match well to what we originally designed. When all the phantom parts are ready, we can put skin material on top of it. We cast the skin material on top of a metal plate that had 5 mm Styrofoam borders taped on it. This way we get different sized pieces of skin material that has smooth surface and thickness is exactly 5 mm. The sizes of pieces were taken from the phantoms

dimensions. Pieces were covered with plastic and they were left hardening overnight. When pieces are ready, they can be placed on top of the phantom and wraped by the plastic film. It was noticed that pieces should not be too big because those are hard to move and wrap. For example making torso from two or three pieces will not be possible, we used six different pieces of skin material to cover the torso. Seams in skin material are easy to fade away because material sticks to itself. Attaching arm to the torso we used acrylic poles that we put inside of torso and arm. For arms stability one round of plastic film was wrapped over arm and torso. Palm was too heavy to be stable with just acrylic poles, so we need to introduce piece of Styrofoam between palm and torso to mechanically support the palm during measurements.

(a) (b)

Figure 20: a) Manufactured phantom structure and b) phantom torso and head with skin material on top.

5 Antenna array measurements

5.1 Design of antenna feed structures and fabrication

To be able to measure the radiation patterns of both co-located and distributed arrays in a realistic mobile platform, we need to design feed networks for the antenna arrays. The arrays are placed on a phone-sized structure, which is 150 × 75 × 8 mm. PCBs were designed to be of this exact size. The microstrip feed lines run from the antenna element at the top to the bottom side of the PCB. This way we get connectors lined up at the bottom of phone and minimize their effect on the operation of the antenna arrays.

For the co-located array, we have two planar array modules that are located in front-left and back-right corners. For the distributed array, we have two modules covering left- and right top corners as was discussed in chapter 2.1 Figure 6. Exploiting the symmetry of the array design, we manufactured only one module of each array and in the measurements, we turned the phone around to realize the other module. Having only one module on the phone chassis allows more space for connectors.

Layer four is the back side, which points to the inside of the phone chassis and is used for the long microstrip feed lines. Layers one and two contain the main and parasitic antenna patches. Layer three is the mutual ground plane for the antenna elements and the microstrip feed lines. The width of the feed lines was calculated with NI AWR TX-line software. To get 50 Ω feed lines at 28 GHz, when using Rogers RO4450B substrate, the width of the lines is 0.208 mm. The minimum distance between feed lines is designed to be the same for all lines. This increases length and amount of turns for some lines, e.g. where it is necessary to reduce electromagnetic coupling between lines. All feed line turns are 90° mitered bends, maintaining good impedance matching of each bend [48]. Between all lines, via stitching was introduced to increase isolation between lines. Via stitching is denser near antenna elements where feed lines are closer to each other, whereas near connectors the line separation is a bit larger. The connectors are evenly positioned at the bottom side of PCB. Figure 21 shows the feed line structure for the co-located array. Figures 21 and 23 show two different cross-sections of PCBs.

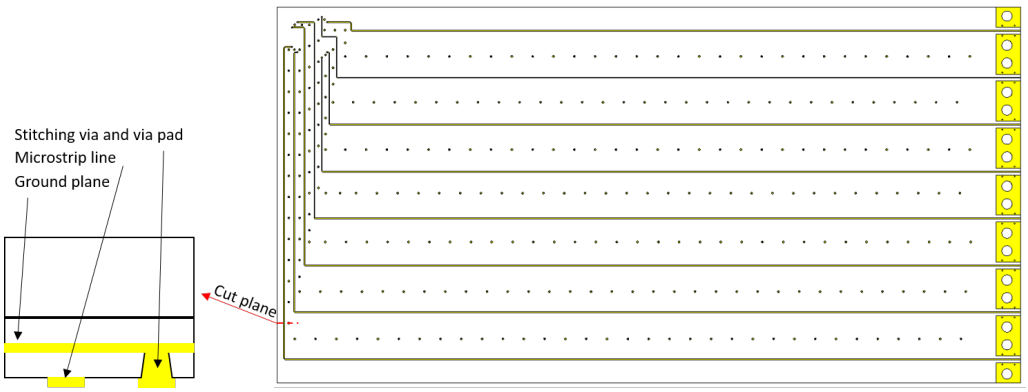

Figure 21: Layer four of the co-located array PCB including feed lines and cross-section of the PCB

For co-located array, we designed PCBs for two different connectors: SMPM connector by Amphenol RF (Mfr. No: 925-169J-51PT, later SMPM connector) and Southwest microwave's narrow block 2.40 mm end launch connector (Mfr. No: 1492-04A-9, later 2.40 mm connector) as shown in Figure 22a and b. The SMPM connector is a small edge mount connector and it is soldered on top of the feed line. This connector is specified up to 40 GHz. With SMPM connectors one needs patch cables to be able to connect them to the antenna measurement equipment. The 2.40 mm connector is screwed on top of feed line and it does not need soldering. This connector allows connecting standard connectors as used in our measurement equipment and hence we do not need any extra cables for connecting. A piece of FR4 PCB was taped to the backside of PCB merely to strengthen the phone structure. A piece of 5 mm thick Rohacell Styrofoam was placed between antenna PCB and FR4 to obtain wanted 8 mm thickness of phone chassis.

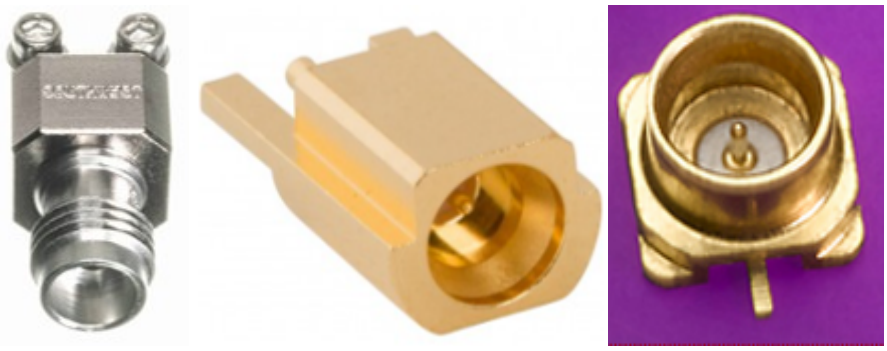

(a) (b) (c)

Figure 22: a) Southwest microwave 2.40 mm narrow block end-launch connector, b) Amphenol RF end-launch connector and c) Molex SMP connector.

To be able to manufacture the distributed array, four different PCB's were designed. One antenna element and its two feed lines were placed on each PCB. Figure 23 shows the feed structure of all PCB panels constituting the distributed array. We can see that for the top- and side element panels, the use of edge or end launch connectors was not possible because all the connectors needed to be inside the phone structure or at the bottom edge. Therefore, the top- and side panels we use Molex SMP (Mfr. No: 85305-0232, later SMP connector) connectors that is shown in Figure 22c. These connectors introduce a 90° turn and allow the patch cable fits inside of the phone. For the front- and back panels the same SMPM connectors were used as in the co-located array. A piece of 5 mm thick Rohacell Styrofoam is placed inside the structure to support four panels and all adjacent mechanically aligned with help of Kapton tape.

Long feed lines introduce extra losses to the measured realized antenna gain. The simulated feed line loss without connector or patch cable are shown in Figure 24. For the co-located array the feed lines cause 4.3 - 6.5 dB of extra loss, and for the distributed array 1.5 - 4.7 dB of extra losses to each antenna element compared to the case without any feed lines. These losses need to be de-embedded after the

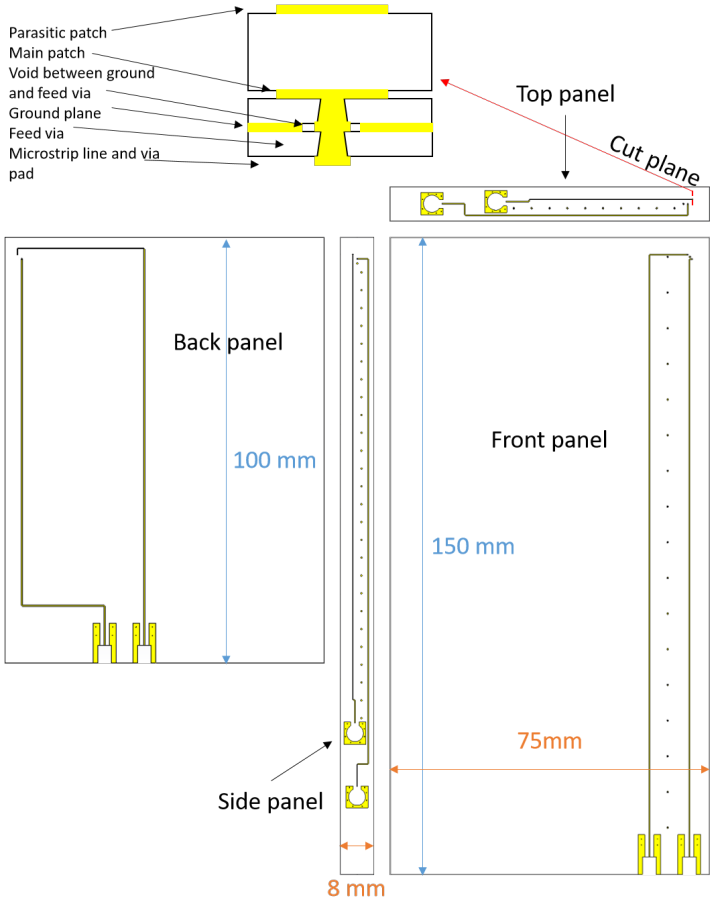

Figure 23: Layer four of the distributed array PCB including feed lines and cross-section of the PCB at the antenna element

antenna measurements to be able to compare measured and simulated realized gain consistently.

Manufacturer of the PCB's had some restrictions on the designs. Because our feed vias and via stitching connects two inner layers, all the vias needed to be made by laser drill, limiting via-hole size to 0.125 mm. This increased the size of each feed via little bit compared to original antenna element shown in chapter 2.1. Moreover, as our stack-up is not symmetrical, boards will slightly bent during the manufacturing process. This does not cause problems with our designs because the boards are very thin so each PCB can be straightened when we assemble the "phone". In addition, we do not have any other components than connectors to add, which the warping of the board does not affect. To counter-effect this bending we taped a piece of FR4 to the backside of the co-located array PCB to support and straighten the PCB's. For the distributed array, we do not need any extra support because all four panels will support each other.

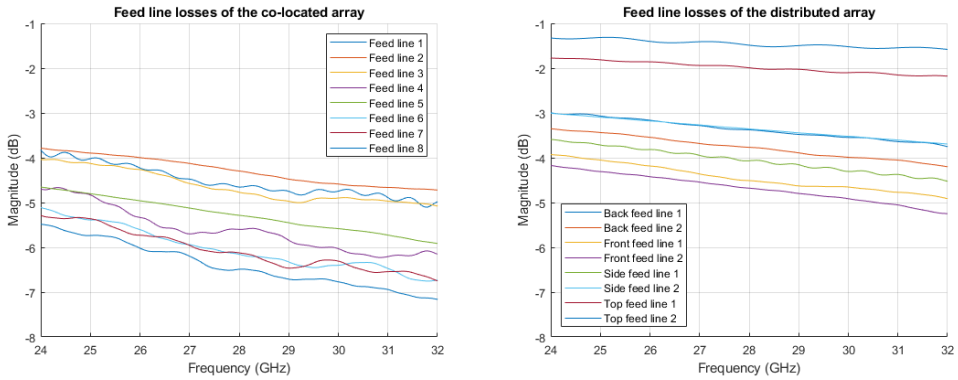

(a) (b)

Figure 24: a) Simulated feed line loss of co-located array, b) Simulated feed line loss of distributed array. Both losses do not contain losses caused by connectors and patch cables.

5.1.1 Selection of the connectors

When we measured the S_{11} of the co-located array with SMPM connectors, S_{xx} ($x = 1 \ldots 8$) parameters did not show any resonance frequency around 28 GHz. We suspected some source of a strong reflection between feed and antennas. This was verified analyzing the wide band refection coefficient in time domain. The Reflection coefficient can be seen in Figure 25, where a clear, strong, reflection at the connector and another reflection from antennas where observed. Reflection from the antenna

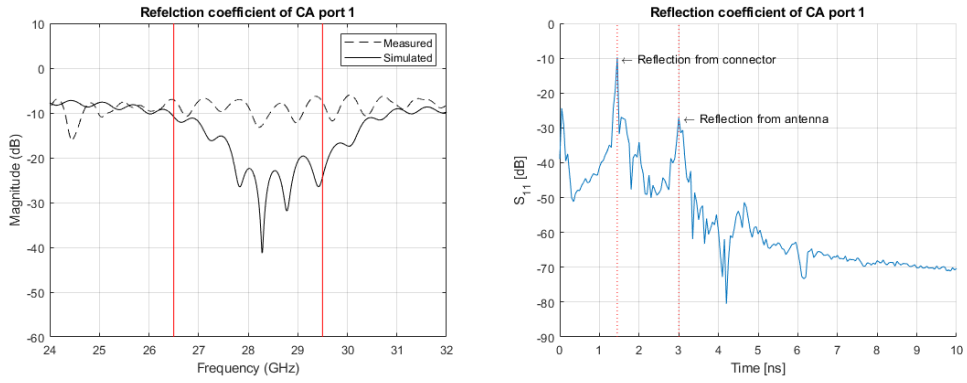

(a) (b)

Figure 25: reflection coefficient of co-located array port 1 a) frequency - and b) time domain.

is much weaker than the reflection from the connector. In frequency domain, the reflection from the poor-quality connector hides the antenna resonance. From a planar near field measurement of the upper side of the PCB, we obtain Figure 26 that shows normalized near-field amplitude distribution. The connector is radiating approximately 10 dB lower level than our antenna. In the far field pattern of this

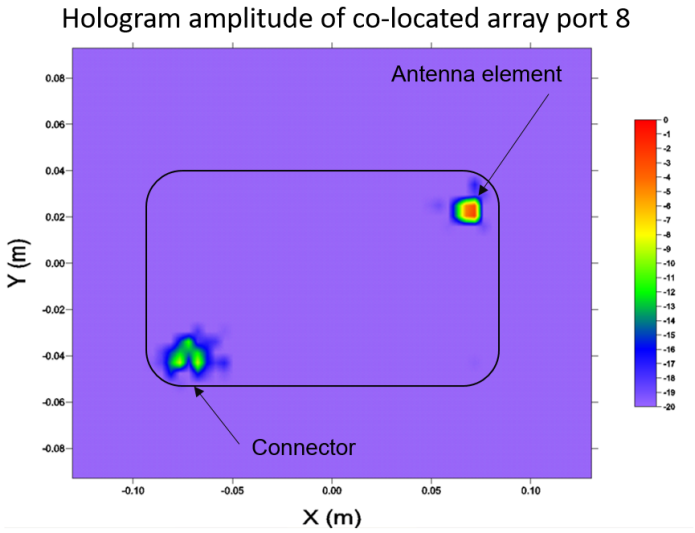

Figure 26: Near field hologram of the co-located array port 8 with SMPM connectors

structure, it would appear as if antenna array of two elements is radiating. If one would like to use these SMPM connectors there should be absorber on top of them during measurements. Absorber will not compensate losses introduced by connectors but it will block radiation. For the co-located antenna array we therefore decided to use only 2.40 mm end launch connector, which does not have this problem.

5.2 Measurements of circuit and free-space parameters

5.2.1 Impedance matching

For antenna measurements, two different setups are used: one is to measure the impedance matching of the antenna elements, including the feed network. The other setup is needed to measure radiation pattern.

For the distributed array, we could measure the impedance matching only of side- and top panels because back and front panels required the use of SMPM connector and ports of those panels do not show any resonance as was discussed in chapter 5.1.1. The measured reflection coefficients of antenna elements on the side and top panels can be seen from Figure 27. The measured matching includes patch cable and connector that we did not have in the simulation, which we need to compensate later. The measured reflection coefficient matched well with the simulated ones. Measured reflection coefficient oscillates more than simulated one but this can be caused by patch cable and connector. Isolation also oscillates and amplitude level is lower than simulated ones. This means that we have extra losses compared to the simulation.

The matching of the co-located array was measured with 2.40 mm end launch connectors. Figure 28 shows the S-parameters of the co-located array. We see a 400-500 MHz frequency shift between measurements and simulations in all ports of the co-located array. On the other hand, the distributed array side- and top panels do not show the same shift. One reason for this frequency shift could be that

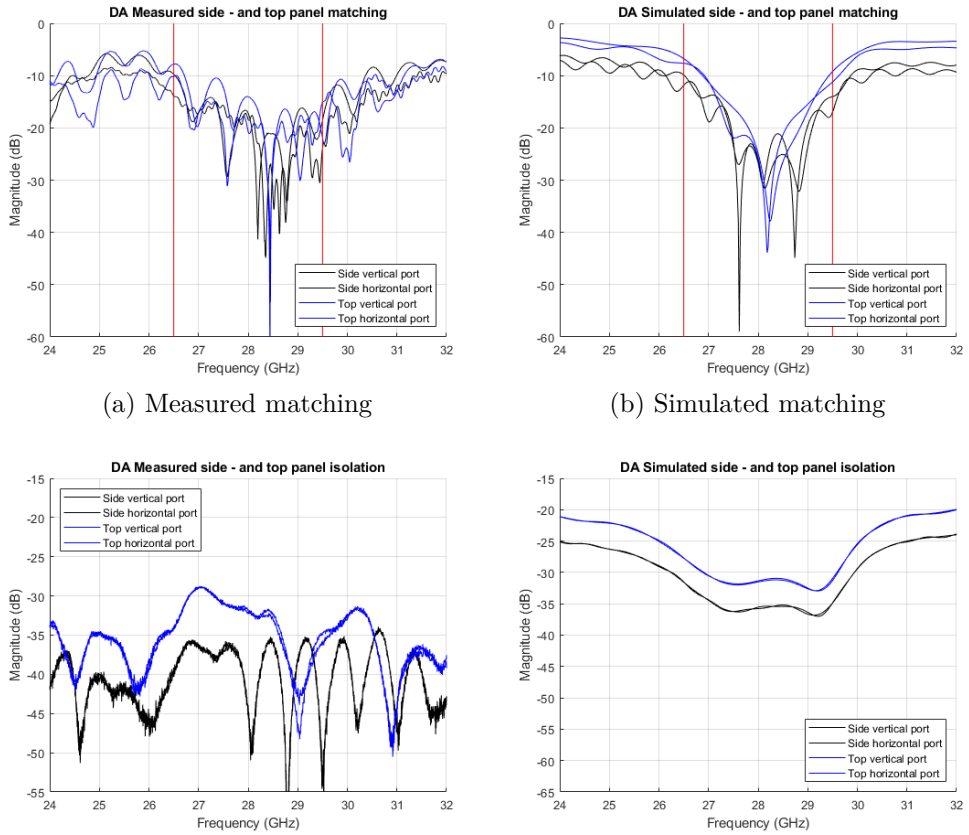

(a) Measured matching

(b) Simulated matching

(c) Measured isolation

(d) Simulated isolation

Figure 27: Distributed array matching and isolation.

our substrates, that was used in fabrication, permittivity was not exactly what we simulated. Losses introduced by soldered connectors in the distributed array could change the observed resonance to lower frequency and make matching look better than it actually is. S_{xy} $(x \neq y)$ parameter show isolation between ports. Isolation is better than -40 dB for all ports, indicating negligible coupling between lines. These results would recommend to measure at 29 GHz rather than at 28 GHz because co-located array has stronger resonance at 29 GHz. It is important to remember that we have long feed lines and reflection introduced by them will dominate the S-parameter.

5.2.2 Radiation patterns of each antenna element

For radiation pattern measurements, we used an anechoic chamber developed by Antenna Systems Solutions (ASYSOL). Key parts of anechoic chamber are VNA, probe antenna and mechanical rotator. In practice, we measure S_{21} of the whole system. Standard gain horn is used as reference antenna to calibrate the system to get realized gain of the antenna under test. To be able to do beam forming we need to measure full radiation patterns of all antenna feeds separately. Orientation of antennas during measurements is shown in Figure 29.

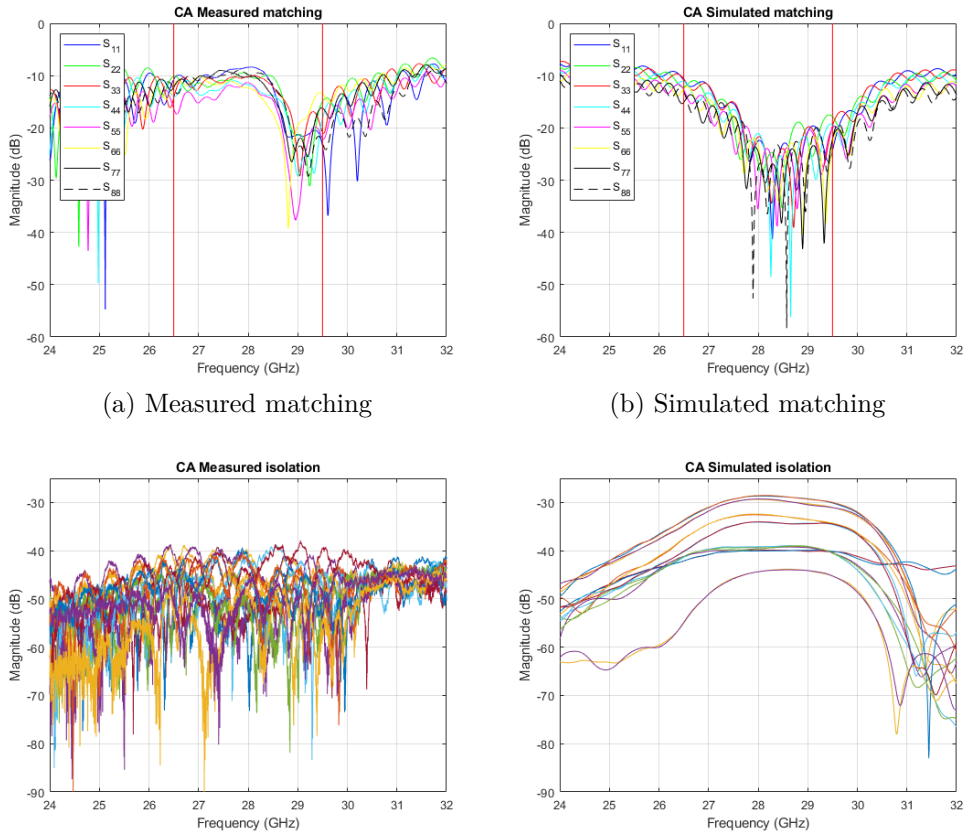

(a) Measured matching

(b) Simulated matching

(c) Measured isolation

(d) Simulated isolation

Figure 28: Co-located array matching and isolation.

The co-located array is placed on top of a plastic holder so that elements are looking towards probe antenna. It was necessary to place the distributed antenna array sideways because we have antenna elements around corners. The sideway placement was only the feasible installation where all feeds can be measured at the same position. A holder for distributed array is same plastic holder as we used with the co-located array with Styrofoam blocks. We use Styrofoam because it does not affect to the radiation but is hard enough to hold the "phone" in its place.

In our anechoic chamber, we need to decide one axis as step-axis and other as scan-axis. Step-axis was decided to be ϕ and as scan-axis θ direction. Figure 30 shows simulated spherical coverage of co-located array with different angular density. We measure radiation patterns with $\phi = 10°$ as smaller ϕ step does not change the resulting CDF of spherical coverage. θ steps can be $1°$ as reducing scan-axis density does not save time. The 3-D pattern was measured in polar coordinates at $\theta = -180°, -179°, ..., 178°, 179°$ and $\phi = -90°, -80°, ..., 70°, 80°$ and transformed to the standard spherical coordinate system. We will lose information of full pattern this way but it should not affect to the spherical coverage and it saves lot of time in the measurements.

Radiation patterns of all ports in the co-located and the distributed arrays were

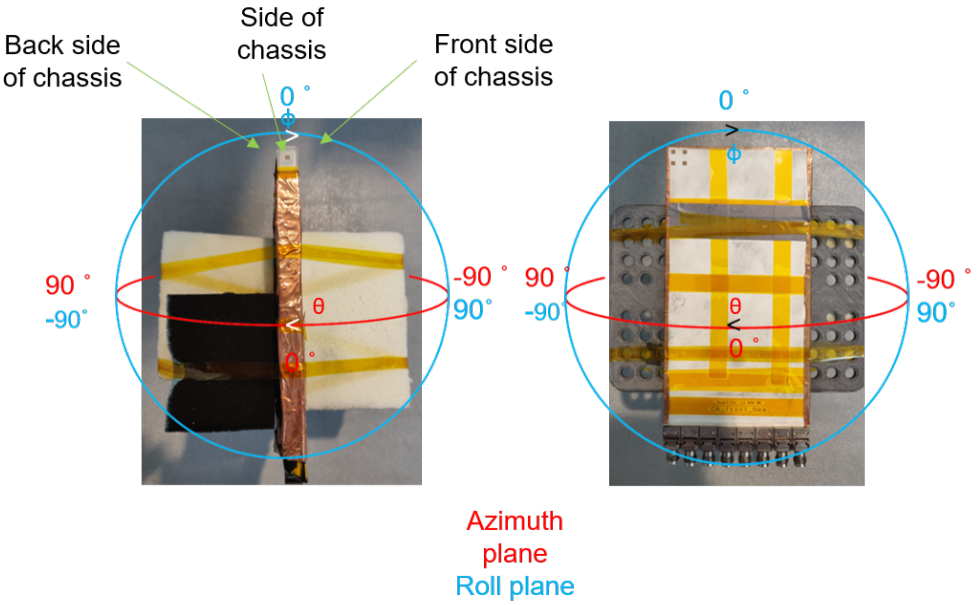

Figure 29: Antenna orientation during free space measurements. Red circle represent θ and blue circle ϕ direction and rotation direction is shown by white arrow

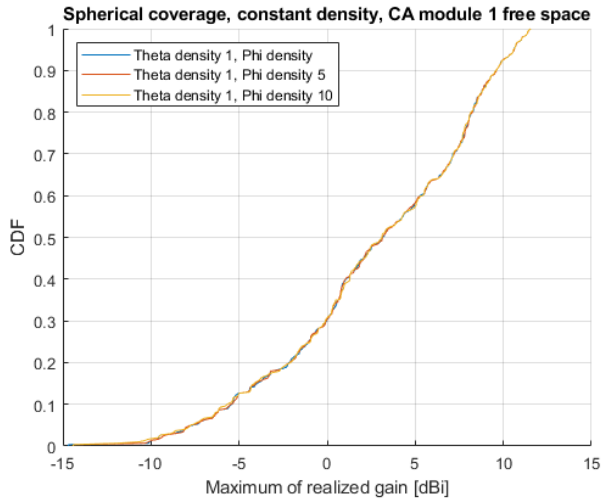

Figure 30: CDF of spherical coverage of simulated co-located array with ϕ density of 1, 5, 10 degrees

measured in free space. Figures 31 and 32 show azimuth cuts ($\phi = 0°$ and $180°$) of radiation pattern of the co-located array ports 1, 2, 7 and 8 and the distributed array back and side ports (plots of radiation patterns of all ports can be found from appendix B). Because $0° \leq \theta \leq 180°$, azimuth cuts are in polar coordinates to be able to present full cuts. We measured only module 1 in free space because module 2 is looking towards the measurement tower. Measurements were performed 28, 28.5 and 29 GHz. The 28 GHz measurement was best in the terms of gain and hence one introduced in the following sections of this thesis.

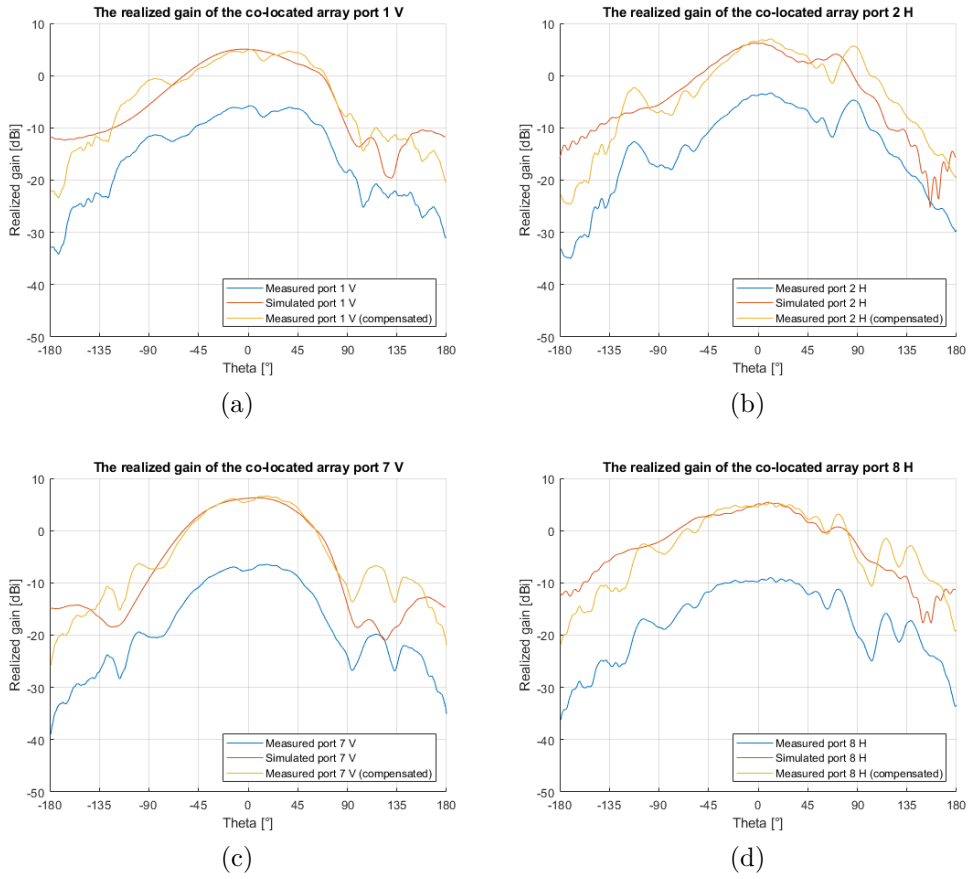

Figure 31: Azimuth cut of realized gain pattern of co-located array ports a) 1 V, b) 2 H, c) 7 V, d) 8 H; "V" and "H" denote that the corresponding feed mainly radiates vertical or horizontal polarization, respectively

From azimuth cuts of realized gain pattern of the co-located array, can be seen that measured pattern ripples more than simulated values but shapes are close to simulated gain patterns. Gain patterns of the co-located array has periodic ripple in horizontal ports (ports 2, 4, 6 and 8). This ripple is caused by surface waves that are traveling away from top edge of the panel and are exiting from left corner of PCB. A copper tape was placed over the sides of the phone chassis. That works as a ground plane and prevents fields exiting from PCB. This does not fully eliminate the ripple but it made ripples smaller. For the distributed array parts of main lobes of front, top and back elements are shadowed by a measurement tower. Especially in patterns of back element, ripples caused by the holder, whose bottom side is plastic, reflects some of radiation although we added absorbers to prevent this.

In theory we could measure all the losses caused by connectors, patch cables and feed lines. However, in practice, for example manual soldering introduces slightly different losses for every connector. It is therefore decided to estimate the loss of cables and connectors and de-embed them by calculating difference between simulated and measured far field in free space. This is done to normalize the measured array

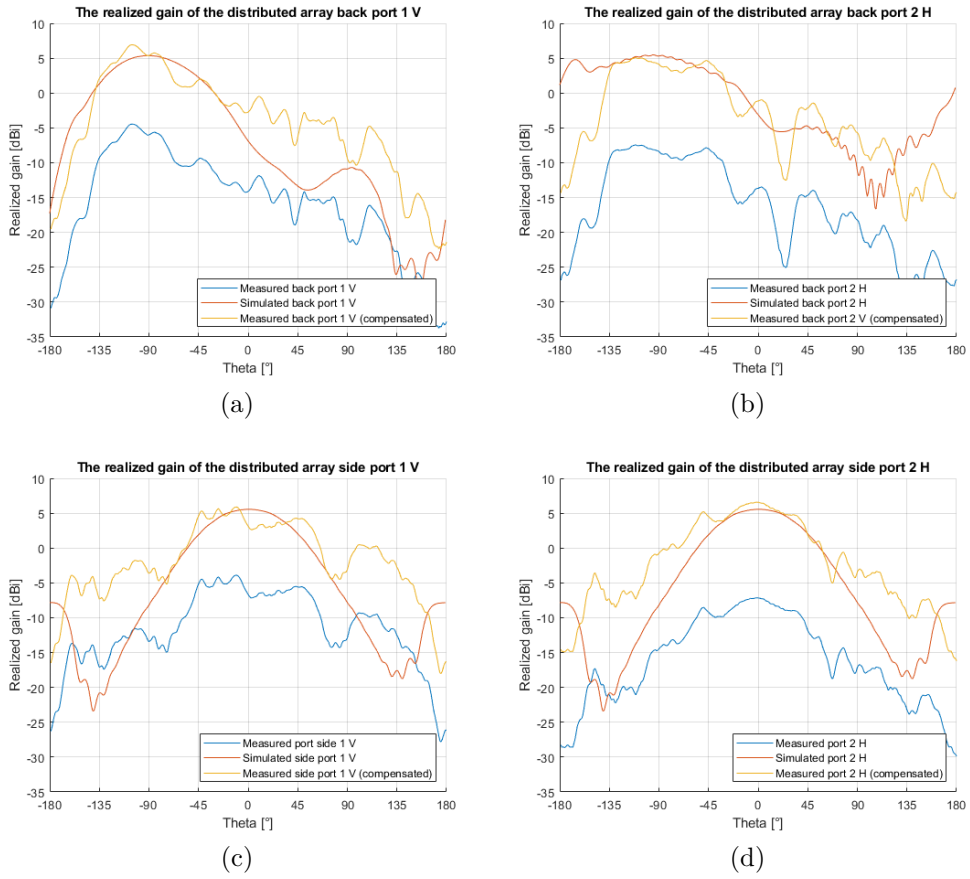

Figure 32: Azimuth cut of realized gain pattern of distributed array a) back 1 V, b) back 2 H, c) side 1 V d) side 2H; "V" and "H" denote that the corresponding feed mainly radiates vertical or horizontal polarization, respectively

to same level with simulated ones. We calculated mean difference of the main beam direction over $\pm 60°$ in both θ and ϕ direction in free space to come up with amplitude compensation terms for losses introduced by cables and connectors of each feed line.

After de-embedding, especially back lobe levels of the top panel of the distributed array are higher than simulated. If we compare difference to simulated arrays, that has no feed network, we see difference from 9.8 up to 17.9 dB for co-located array and from 7.4 up to 16 dB for distributed array, both without de-embedding, in the main lobe direction and depending on the feed line. These differences contain losses due to connectors, patch cables, manual soldering and manufacturing errors etc. It is possible to simulate feed line losses but other losses are unknown. Table 2 shows correction terms for amplitudes of all ports, which are also used in phantom measurements to correct the measured gain.

	Port 1 V	Port 2 H	Port 3 V	Port 4 H	Port 5 V	Port 6 H	Port 7 V	Port 8 H
CA	10.6881	10.3864	10.2697	10.9780	12.4442	12.0777	13.1049	14.4027
	Back V	Back H	Front V	Front H	Side V	Side H	Top V	Top H
DA	11.1675	11.6131	15.3145	14.6299	10.6729	15.2698	9.5229	9.0250

Table 2: Gain correction terms to de-embed losses of cables, connectors and feed lines for co-located and distributed array in dB

5.3 Radiation pattern measurements with phantom

Radiation pattern measurements under the presence of the body phantom were performed for two modules of both arrays. Figure 33 shows orientation of phantom during the measurements. Phantom's back side is seen in the Figure 33 and it is attached from bottom to the measurement tower so that it shadows only a small area of the solid angle where legs should be. That is a direction where antennas do not radiate and shadowing of the tower is not supposed to have big impact on evaluation of gains.

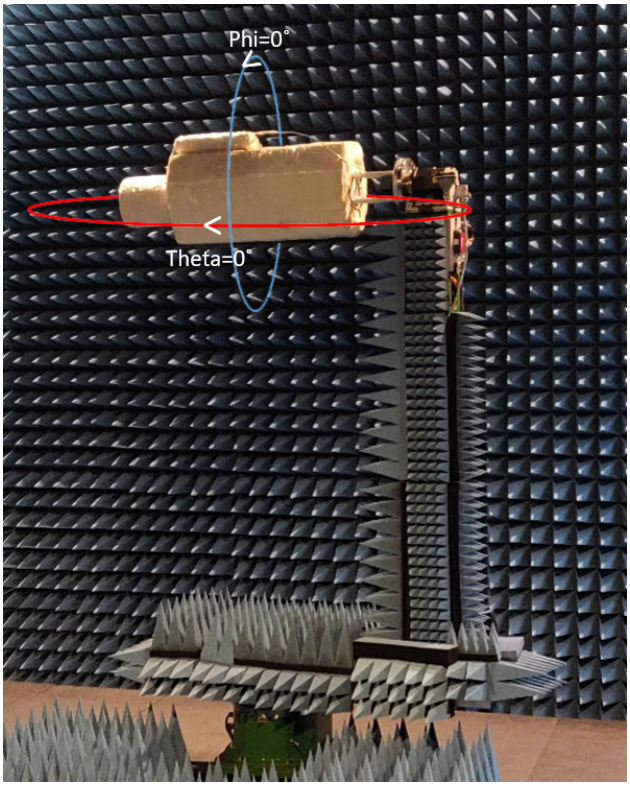

Figure 33: Phantom orientation in the measurements. Phantom is at position $\theta = 90°$, $\phi = -90°$

Because phantom is not point source, we have new uncertainties in the measurements. Biggest error factory is uneven illumination of phantom by the probe antenna. This means that the probe antennas gain is not constant while moving sideways from

the center of rotation. The error caused by uneven illumination can be as high as 1 dB with our measurement setup. We did not measure this error and it is bigger when object is feather away from center of rotation. This will add our measurement uncertainty.

Because of the phantom orientation, we measure only 36 points on the azimuth cut during the full-3D radiation pattern measurement, because we measure ϕ-direction only every 10°. We decided to measure azimuth cuts separately. This way we can increase amount of points in the cuts. Figure 34 shows realized gain patterns of ports 1, 2, 9 and 10, both azimuth ($\theta = 90°$) and elevation cuts ($\phi = 90°$ and 180°) of the co-located array. In the co-located array module 1 consisting at ports 1 – 8 is looking towards phantom and module 2 made of ports 9 – 16 is looking away from the phantom. Azimuth and elevation cuts of all ports can be seen from appendix C.

Measured patterns from the co-located array with phantom match well to the simulated ones. In elevation cuts, measured results do not get as low values as simulated results because dynamic range of our measurement system is not enough. Also, measured patterns from ports 9, 11 and 12 decays earlier, around $\theta = 100°$. Azimuth cuts of realized gain pattern from ports 1-8 show that dip caused by phantom is shifted by $\sim 5°$ probably because of misplacement of phone compared to the phantom torso. Another possible reason is angular error caused by phantom, as it is not a point source on space but over 80 cm long radiation source. This can cause up to 4° error in θ direction with our measurement setup. Azimuth cuts of module 2 matches well with simulated patterns because this module is looking away from the phantom and is radiating almost like in free space. Average difference between measured and simulated patterns is between $0.5 - 7.3$ dB depending on the antenna feed. This non-negligible difference is caused mostly by limited dynamic range of measurement system. Due to this limitation in dynamic range, antenna gain estimation in the shadowed angular region of the phantom are inaccurate and significantly different from what was simulated. The co-located array was measured with phantom twice separately to conform repeatability of measurement. Between the measurements, the phone chassis was detached from the palm after measurement of each module. As Figure 34 shows, there is a minimal difference between two measurement sets, indicating good repeatability with our phantom.

Figure 35 shows azimuth and elevation cuts of module 1 front ports and module 2 top ports in the distributed array. Front ports from module 1 are on left side of the phone-chassis looking towards phantom while module 2 top ports are on the right side of the chassis looking upwards. Elevation cuts match well with simulated results. Measured radiation patterns show limited dynamic range and hence the gains that phantom is shadowing are not as accurate as simulation. Otherwise, measured elevation cuts look similar to simulations. Azimuth cuts from front element in module 1 looks almost the same as simulated cut. The same angular difference at the shadowed area caused by phantom can be seen also in the distributed array patterns as was seen in the co-located array patterns. Measured azimuth cut of vertically polarized port from the top element at the module 2 has higher gain near shadowed region that we simulated. This could be caused by a few degrees at error in tilt angle of phone. Also at elevation cut of horizontally polarized front port on

module 2 shows ~ 5 dB difference near $0°$. This means the antenna radiates more upwards, which could be caused bigger tilt angle. Although there is some differences in patterns between measurements and simulations, they are still close to each other. Errors between simulated and measured gain patterns is in average between $0.6 - 5.6$ dB depending on the antenna feed. The largest error is mostly caused by limited dynamic range of the measurement system.

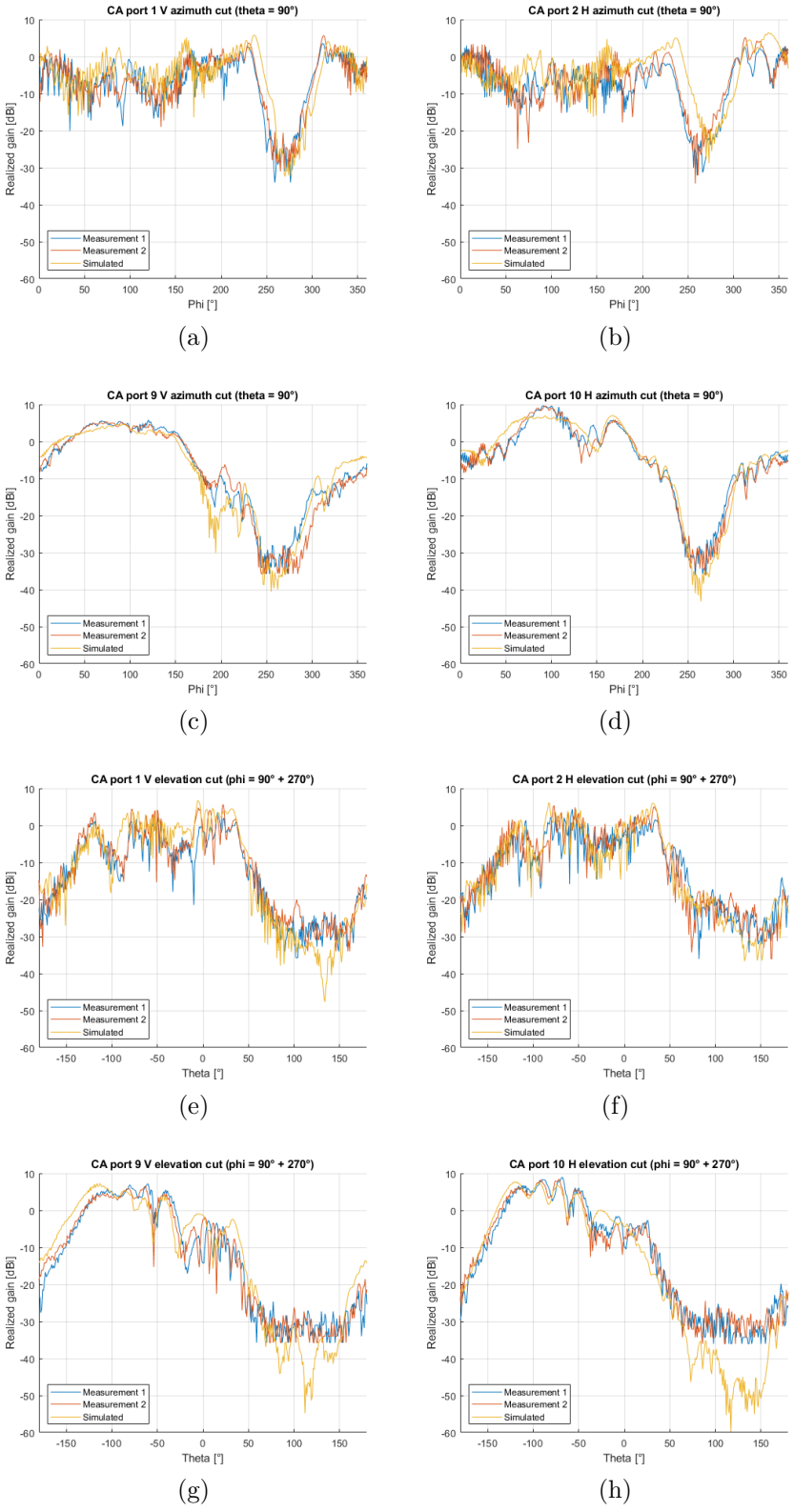

Figure 34: Azimuth and elevation cuts of realized gain pattern of the co-located array with phantom.

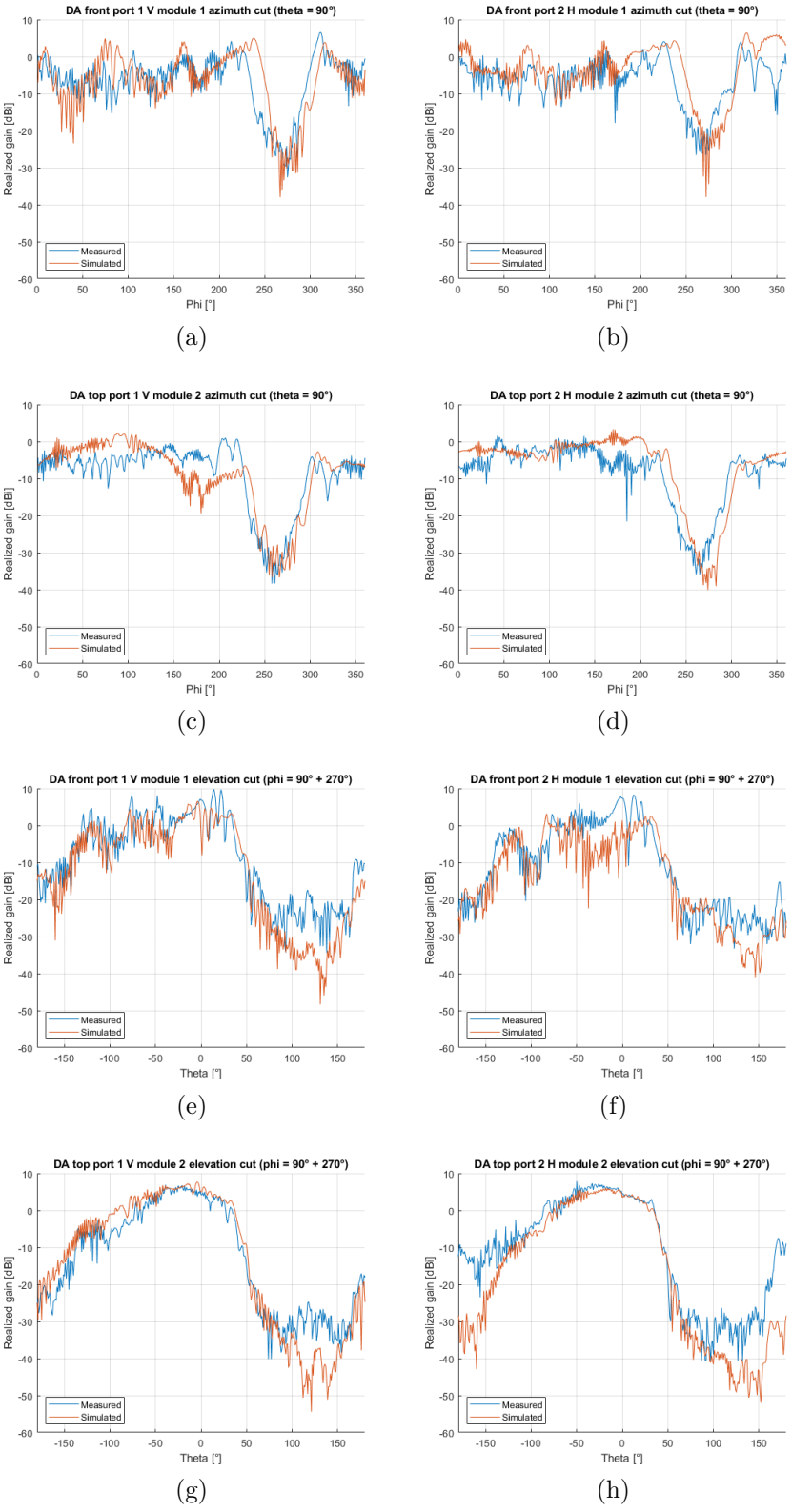

Figure 35: Azimuth and elevation cuts of realized gain pattern of the distributed array with phantom.

5.4 Beam synthesis

Beam forming is applied to measured and simulated radiation patterns. As mentioned in chapter 4.1.2 we use ideal three-bit phase shifter to realize 512 beams in total. These beams are affected by small-scale fading because radiation is coming, especially with phantom, from multiple reflections. These multipath components are summed up and they cause fast and time varying fluctuation to the amplitude. Averaging amplitude over $\pm 5°$ azimuth and polar angles reduces effect of small-scale fading and allows better comparing between measurements and simulations. We did averaging only over azimuth angels because we measured every 10° in polar direction. After the averaging is applied to every beam, maximum realized gain for a pointing angle is chosen from the beams. Figure 36 shows maximum of realized gain over whole solid angle from the co-located and the distributed arrays in free space.

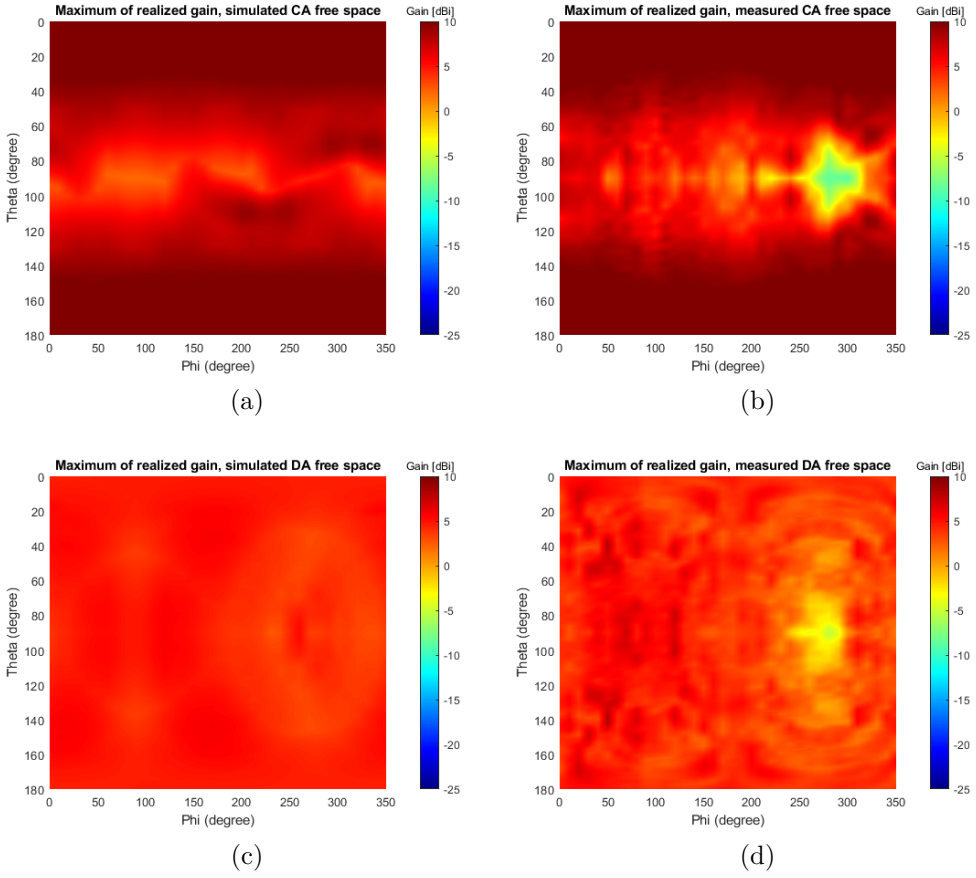

Figure 36: Maximum of realized gains of the a) simulated co-located, b) measured co-located, c) simulated distributed and d) measured distributed array in free space. The broadside direction is $\theta = 0°$ direction for co-located array module 1.

Both the co-located and the distributed arrays had a block of absorber to cover connector during the measurements. This absorbers effect can be seen in $\theta = 90°$, $\phi = 270°$ direction as an area where clear null appears in the pattern. The angular distribution of maximum gain pattern for the co-located array looks similar to

simulated pattern. Near $\theta = 90°$ the measured gain is lower than in simulation but the gains in the main beam directions are looking similar between measured and simulated patterns. Distributed array has ripples in the distribution, which cannot be seen in the simulated results. This was expected because the individual measured radiation patters of distributed array had also much more ripples than simulated radiation patterns. Maximum gain of distributed arrays is higher and minimum is lower in the measured pattern than simulated one. This difference will be seen also in spherical coverage.

Figure 37 shows maximum realized gain of the co-located and the distributed array over solid angle with a human phantom. With the co-located array, there is a few clear differences between measurements and simulation. For example, measured peak gain is not as high as simulation. As seen from $\theta = 90°$, $\phi = 90°$ areas which show smaller gain in measurements than in simulations. Other difference of gain distribution is diffraction over phantoms head. In measurements, we do not see clear diffraction effect over phantoms head probably because our material reflects more energy than in simulation. Still some diffraction over the head is seen especially in measurement 2. Also some radiation that cannot be seen in simulations is present in measurements when $\theta < 20°$, most likely due to an error in phones tilt angle. In these plots shadowing effect of the measurement tower is the region below $\theta = 150°$. When calculating CDF of spherical coverage we could drop this area away because it is affected by the measurement system. The maximum gain distribution of the distributed array differs also from simulated results. The measured gain pattern is not as steady as it is in simulations. In simulation realized gain is ~ 5 dBi when $\theta < 110°$ but in measurements the gain varies. With the distributed array, the area which is shadowed by the tower seems to be larger than it is with the co-located array.

Spherical coverage CDF of both co-located and distributed array in free space can be seen from Figure 38. As it was expected from Figure 36 there is only a small difference between measurements and simulations. Measured CDF for the co-located array matches with simulated one until 0.6 probability level. The measured starts to get smaller gain values. For example at 0.1 probability level there is 2.2 dB difference between measured on simulated results.

The distributed array has much more differences between measured and simulated free space result than co-located array. Measured peak gain is 2.6 dB higher than simulated one but after 0.86 probability level measured gain starts to be smaller than simulated ones. At 0.5 and 0.1 probability levels, measured gains are 0.7 and 2 dB lower than simulated ones. This was expected result after the maximum of realized gain plots.

Spherical coverage CDF of co-located and distributed array with phantom are shown in Figure 39. For the co-located array, shapes of spherical coverage CDF curves are similar between measurements and simulation and difference is small. There is less than 1 dB difference between two measurements indicating good repeatability of measurements. The difference between measured and simulated peak gains is 2 dB's and at 0.5 and 0.1 probability level difference are 0.6 and 0.2 dB, respectively, indicating that the numerical simulation of scattered filed from the co-located arrays

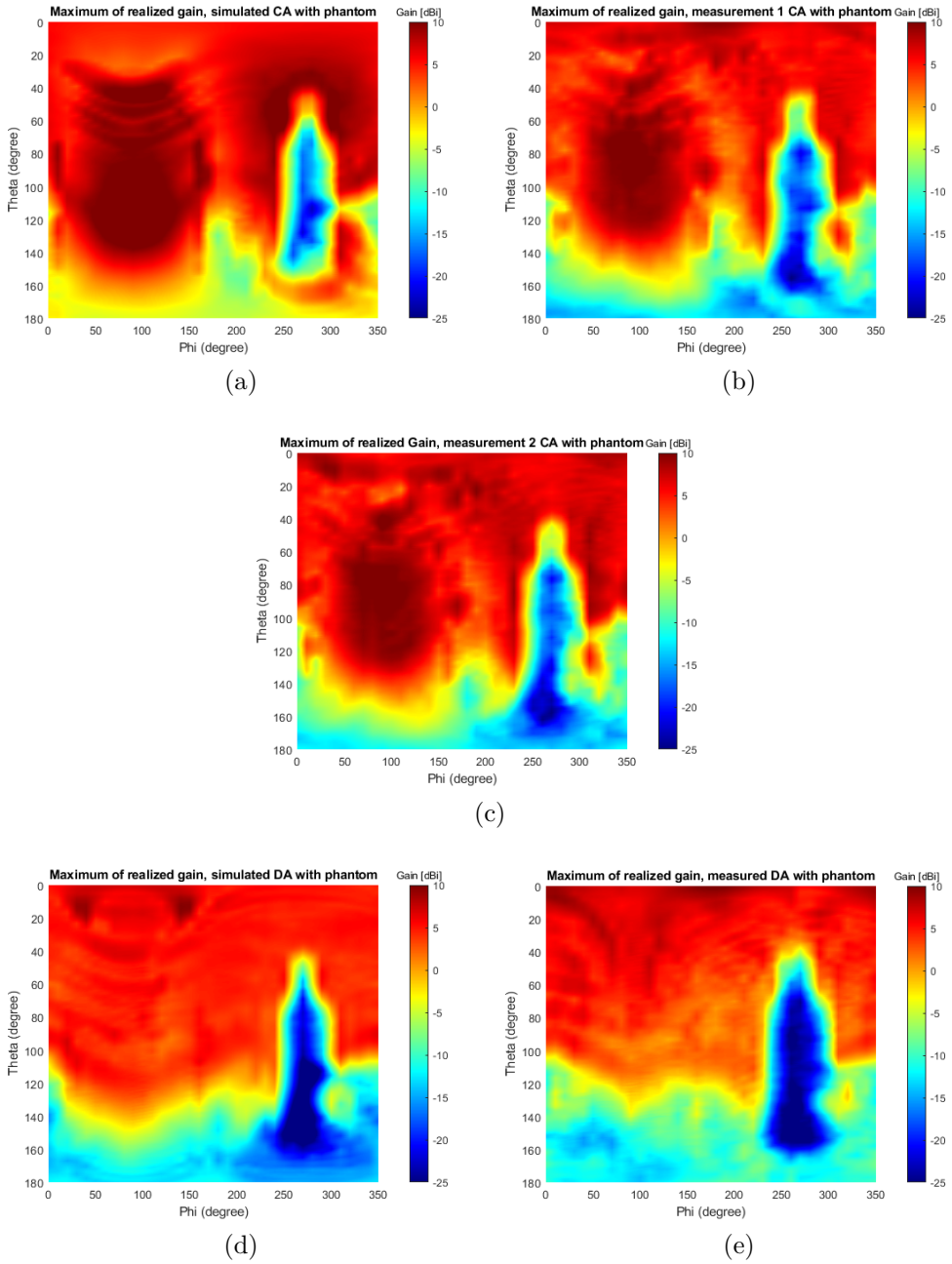

Figure 37: Maximum of realized gain of the a) simulated co-located, b) measurement 1 co-located, c) measurement 2 co-located, d) simulated distributed and e) measured distributed array with phantom.

under the presence of human phantom is sufficiently accurate. Figure 39b show spherical coverage CDF of the distributed array with phantom. Although measured and simulated results of the distributed array had big difference in free space, they are closer with phantom. Measured gains drop faster than simulated ones, which could be seen also from Figure 37. Although CDF curves have offset to each other,

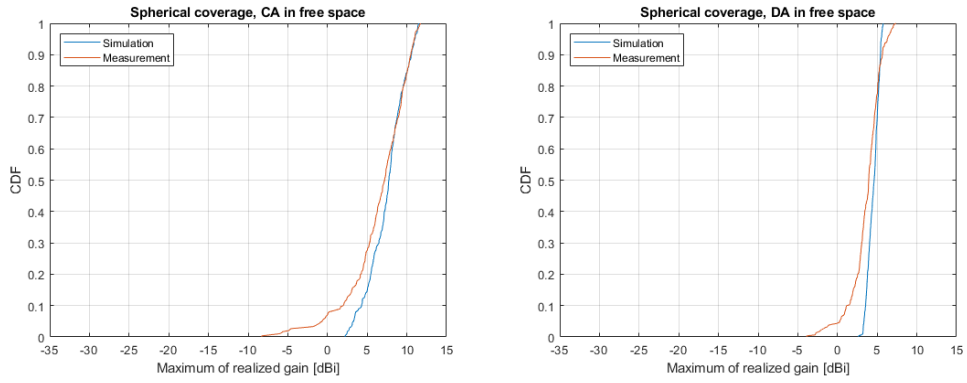

(a) (b)

Figure 38: Spherical coverage CDF of measured and simulated a) co-located and b) distributed arrays in free space.

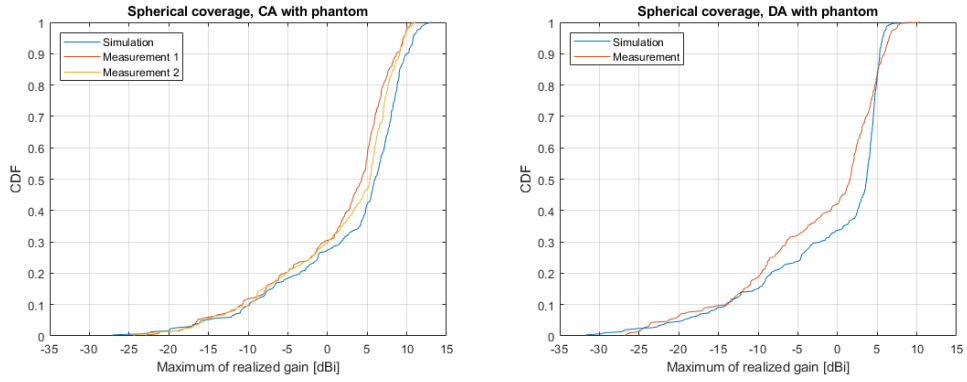

(a) (b)

Figure 39: Spherical coverage CDF of measured and simulated a) co-located and b) distributed arrays with phantom.

the shape of curves are close to each other. The peak gain is bigger in measured results than in simulated by 0.9 dB, at 0.5 and 0.1 probability levels measured level is 2 and 0.2 dB lower than simulated, respectively.

It is fair to say that we get same spherical coverage CDF from measurements and simulations with the co-located array. With the distributed array we have little slightly more between measurements and simulations but still they are close to each other. Simulation model used in this work is approximation and functionality of it has not been shown with measurements previously. The phantom has material on top of it, which mimics human skin, and measurements are done with good manor. Measured and simulated spherical coverage CDF agrees well which indicated that simulation model is accurate enough and measurement setup works as planned.

6 Conclusions

6.1 Summary of works

In chapter two, different antenna elements that has proposed to a mobile use at 28 GHz was introduced. Electromagnetically coupled stacked patch antenna element was introduced and chosen as antenna element for this thesis. Matching and radiation patterns of the single stacked patch element was simulated an shown. Phased antenna arrays were introduced, two different antenna arrays were created using stacked patch antenna element and beamforming was discussed. After creating the antenna arrays spherical coverage and total array gain were derived for antenna array evaluations.

At the beginning of chapter three, different human models used in previous studies was shown. Different approaches to mimic humans effect to the radiation of mobile antennas was introduces, but most of them are simulation methods. It was shown that in measurements actual human is used which increases the measurement error and repeatability suffers. It was shown that measurement with human phantom across the whole solid angle has not done. In the end of chapter, electrical properties of human tissues was discussed and study made by Gabriel et al. was introduces. Using their permittivity model of skin, it was shown that electromagnetic waves at 28 GHz do not penetrate skin. To mimic skin of human two skin phantoms, gelatin and polyethylene based skin phantoms, were shown and differences of them was discussed.

Chapter four introduced simulation and evaluation method for antenna arrays. Simplified human phantom was introduced and by using the evaluation method compared using spherical coverage to the accurate human model. It was shown that the simplified human phantom mimics human well in terms of spherical coverage. Polyethylene based skin material for phantom was discussed in detail, it was manufactured and its dielectric properties was measured and shown its permittivity is similar with human skin. Finally, simplified phantom was manufactured from Styrofoam and skin material was added on top of it.

Manufacturing of co-located and distributed arrays was described at the beginning of Chapter five. Measurement setups for impedance matching and over-the-air measurements was introduced, measurements in free space were performed and de-embedding losses of feed lines and measurement cable was calculated from measured realized gain patterns to normalized differences between measured and simulated patterns. Measurements with phantom was described, performed and realized gain patterns was shown to have good agreement between measurements and simulation. Finally, beam synthesis was performed and our two antenna arrays were compered to simulations through maximum of realized gain and spherical coverage. Spherical coverage shows less than 2 dB difference between measurements and simulations, which is good agreement.

6.2 Key findings

Finding 1: Material that mimics human skin across the frequency band from 5 - 20 GHz was manufactured. Dielectric properties were experimentally shown to be close to those of human skin.
Evidence: Figure 18 shows real and imaginary parts of the permittivity of the manufactured skin-phantom material at 5 to 20 GHz measured several times during a four month period. We can see a good agreement between the permittivity of manufactured material and of human skin. Also we concluded that the lifespan of the manufactured material is up to three months

Finding 2: Antenna measurements with the fabricated phantom are accurate enough to determine the spherical coverage, and those measurements are also repeatable.
Evidence: Figure 39 show the CDF of spherical coverage of two manufactured antenna arrays at 28 GHz. The differences between simulated and measured results is 2 dB at maximum. Furthermore, in Figure 39a we see the CDFs of two separate measurements with the same array and phantom, and the difference between two measurements is less than 1 dB, which indicated a good repeatability of the measurements.

Finding 3: The simulation method presented in Section 4.1.2, that is used to quantify the antenna-human body interaction at 28 GHz, is valid.
Evidence: In Figure 39 the differences between simulated and measured spherical-coverage results for the same antenna and body phantom are less than 2 dB, which is a very good agreement in view of the large phantom size in relation to the wavelength of about 2 mm.

As a final conclusion, in this thesis we presented and validated an experimental method for characterising antenna arrays used in mobile phones at 28 GHz under the presence of the user.

References

[1] Nordic-Baltic Telecom Market, available at https://statistik.pts.se/en/nordic-baltic-telecom-market/.

[2] Tefficient, "Industry analysis 3 2018," available at https://tefficient.com/china-and-india-shift-to-4th-gear-leave-many-mature-markets-in-the-dust/.

[3] S. Zhang, X. Chen, I. Syrytsin, and G. F. Pedersen, "A planar switchable 3-d-coverage phased array antenna and its user effects for 28-ghz mobile terminal applications," *IEEE Transactions on Antennas and Propagation*, vol. 65, no. 12, pp. 6413–6421, Dec. 2017.

[4] C. Gustafson and F. Tufvesson, "Characterization of 60 ghz shadowing by human bodies and simple phantoms," in *2012 6th European Conference on Antennas and Propagation (EUCAP)*, Mar. 2012, pp. 473–477.

[5] B. Xu, Z. Ying, L. Scialacqua, A. Scannavini, L. J. Foged, T. Bolin, K. Zhao, S. He, and M. Gustafsson, "Radiation performance analysis of 28 ghz antennas integrated in 5g mobile terminal housing," *IEEE Access*, vol. 6, pp. 48 088–48 101, 2018.

[6] K. M.N, S. Gillani, M. Jamil, and T. Iftikhar, "Multi antenna systems for 5g mobile phones," *World Academy of Science, Engineering and Technology International Journal of Electrical and Information Engineering*, vol. 12, no. 2, pp. 48 088–48 101, 2018.

[7] N. Mohd Nor, M. h. Jamaluddin, M. Kamarudin, and M. Khalily, "Rectangular dielectric resonator antenna array for 28 ghz applications," *Progress In Electromagnetics Research C*, vol. 63, pp. 53–61, 04 2016.

[8] M. Rutschlin, "5g antenna design for mobile phones monads," *The SIMULIA Blog*, 2019, available at https://blogs.3ds.com/simulia/5g-antenna-design-mobile-phones/.

[9] G. A. T. Warren L. Stutzman, *Antenna Theory and Design, 3rd Edition.* Wiley, 2012.

[10] C. Cziezerski, M. Heino, P. Koivumäkiand K. Haneda, and C. Icheln, "Comparing gains of 28 ghz modular-based phased antenna arrays on a 5g mobile phone," in *APC 2019 : The IET Conference on Antennas and Propagation*, Nov. 2019, pp. 1–5.

[11] D. Pozar, *Microwave Engineering, 4th Edition.* Wiley, 2011.

[12] Z. Wang, Y.-Y. Song, Y. Sun, J. Bevivino, M. Wu, V. Veerakumar, T. J. Fal, and R. E. Camley, "Millimeter wave phase shifter based on ferromagnetic resonance in a hexagonal barium ferrite thin film," *Applied Physics Letters*, vol. 97, no. 7, p. 072509, 2010.

[13] J. Hesselbarth and R. Vahldieck, "Concepts for millimeter-wave waveguide-mems phase shifters," *Microwave and Optical Technology Letters*, vol. 52, no. 5, pp. 1028–1030, 2010.

[14] J. Helander, K. Zhao, Z. Ying, and D. Sjöberg, "Performance analysis of millimeter-wave phased array antennas in cellular handsets," *IEEE Antennas and Wireless Propagation Letters*, vol. 15, pp. 504–507, 2016.

[15] K. Haneda, M. Heino, and J. Järvelaeinen, "Total array gains of millimeter-wave mobile phone antennas under practical conditions," in *2018 IEEE 87th Vehicular Technology Conference (VTC Spring)*, Jun. 2018, pp. 1–6.

[16] K. Haneda, M. Heino, and J. Järveläinen, "Total array gains of polarized millimeter-wave mobile phone antennas," in *2018 European Conference on Networks and Communications (EuCNC)*, Jun. 2018, pp. 167–171.

[17] M. Steinbauer, A. F. Molisch, and E. Bonek, "The double-directional radio channel," *IEEE Antennas and Propagation Magazine*, vol. 43, no. 4, pp. 51–63, Aug. 2001.

[18] J. Järveläinen, K. Haneda, and A. Karttunen, "Indoor propagation channel simulations at 60 GHz using point cloud data," *IEEE Trans. Ant. Prop.*, vol. 64, no. 8, pp. 4457–4467, Aug. 2016.

[19] P. Koivumäki, S. L. H. Nguyen, K. Haneda, and G. Steinböck, "A study of polarimetric diffuse scattering at 28 GHz for a shopping center facade," in *Proc. 29th IEEE Int. Symp. Personal, Indoor and Mobile Commun. (PIMRC'18)*, Bologna, Italy, Sep. 2018, pp. 182–187.

[20] X. Chen, L. Tian, P. Tang, and J. Zhang, "Modelling of human body shadowing based on 28 ghz indoor measurement results," in *2016 IEEE 84th Vehicular Technology Conference (VTC-Fall)*, Sep. 2016, pp. 1–5.

[21] J. Hejselbaek, J. O. Nielsen, W. Fan, and G. F. Pedersen, "Measured 21.5 ghz indoor channels with user-held handset antenna array," *IEEE Transactions on Antennas and Propagation*, vol. 65, no. 12, pp. 6574–6583, Dec. 2017.

[22] K. Zhao, J. Helander, D. Sjöberg, S. He, T. Bolin, and Z. Ying, "User body effect on phased array in user equipment for the 5g mmwave communication system," *IEEE Antennas and Wireless Propagation Letters*, vol. 16, pp. 864–867, 2017.

[23] M. N. Kulkarni, A. O. Kaya, D. Calin, and J. G. Andrews, "Impact of humans on the design and performance of millimeter wave cellular networks in stadiums," in *2017 IEEE Wireless Communications and Networking Conference (WCNC)*, Mar. 2017, pp. 1–6.

[24] M. Heino, C. Icheln, and K. Haneda, "Finger effect on 60 ghz user device antennas," in *2016 10th European Conference on Antennas and Propagation (EuCAP)*, Apr. 2016, pp. 1–5.

[25] R. Khan, A. A. Al-Hadi, and P. J. Soh, "User effect on the efficiency of 4-port mobile terminal antenna at 28 ghz," in *2017 International Symposium on Antennas and Propagation (ISAP)*, Oct. 2017, pp. 1–2.

[26] C. Di Paola, I. Syrytsin, S. Zhang, and G. F. Pedersen, "Investigation of user effects on mobile phased antenna array from 5 to 6 ghz," in *12th European Conference on Antennas and Propagation (EuCAP 2018)*, Apr. 2018, pp. 1–5.

[27] M. Heino, C. Icheln, and K. Haneda, "Self-user shadowing effects of millimeter-wave mobile phone antennas in a browsing mode," in *2019 13th European Conference on Antennas and Propagation (EuCAP)*, Mar. 2019, pp. 1–5.

[28] J. Anguera, A. Andújar, A. Camps, C. Puente, and C. Picher, "Mitigation of the finger loading effect in handset antennas," in *Proceedings of the Fourth European Conference on Antennas and Propagation*, Apr. 2010, pp. 1–4.

[29] Z. Ahmad, *Dielectric Material*. IntechOpen, Oct. 2012, available at https://www.intechopen.com/books/dielectric-material/polymer-dielectric-materials/.

[30] S. Gabriel, R. Lau, and C. Gabriel, "The dielectric properties of biological tissues: Iii. parametric models for the dielectric spectrum of tissues," *Physics in medicine and biology*, vol. 41, pp. 2271–93, Dec. 1996.

[31] S. Alekseev and M. Ziskin, "Human skin permittivity determined by millimeter wave reflection measurements," *Bioelectromagnetics*, vol. 28, no. 5, pp. 331–339, 2007.

[32] M. Lazebnik, E. L Madsen, G. Frank, and S. C Hagness, "Tissue-mimicking phantom materials for narrowband and ultrawideband microwave applications," *Physics in medicine and biology*, vol. 50, pp. 4245–58, 10 2005.

[33] S. Di Meo, S. Morganti, L. Pasotti, M. Conti, M. Pasian, and G. Matrone, "Preliminary experimental characterization of gelatin-based tissue-mimicking materials for realistic breast phantoms aimed at microwave applications," in *2018 EMF-Med 1st World Conference on Biomedical Applications of Electromagnetic Fields (EMF-Med)*, Sep. 2018, pp. 1–2.

[34] T. Wu, T. S. Rappaport, and C. M. Collins, "Safe for generations to come: Considerations of safety for millimeter waves in wireless communications," *IEEE Microwave Magazine*, vol. 16, no. 2, pp. 65–84, Mar. 2015.

[35] F. A. Duck, *Physical Properties Of Tissue: A Comprehensive Reference Book*. Academic Press, 1990, p. 336.

[36] J. Lacik, V. Hebelka, J. Velim, Z. Raida, and J. Puskely, "Wideband skin-equivalent phantom for v- and w-band," *IEEE Antennas and Wireless Propagation Letters*, vol. 15, pp. 211–213, 2016.

[37] N. Chahat, M. Zhadobov, S. Alekseev, and R. Sauleau, "Human skin-equivalent phantom for on-body antenna measurements in 60 ghz band," *Electronics Letters*, vol. 48, no. 2, pp. 67–68, Jan. 2012.

[38] D. Dancila, R. Augustine, F. Töpfer, S. Dudorov, X. Hu, L. Emtestam, L. Tenerz, J. Oberhammer, and A. Rydberg, "Millimeter wave silicon micromachined waveguide probe as an aid for skin diagnosis – results of measurements on phantom material with varied water content," *Skin Research and Technology*, vol. 20, no. 1, pp. 116–123, 2014.

[39] ITU-R Recommendation P.2040-1, "Effects of building materials and structures on radiowave propagation above about 100 mhz," Jul. 2015, available at https://www.itu.int/rec/R-REC-P.2040-1-201507-I/en.

[40] 3rd Generation Partnership Project (3GPP), "Discussion of mmwave ue eirp and eis test," 3GPP TSG-RAN WG4 NR AH Meeting R4-1700095, Jan. 2017, available at https://www.3gpp.org/ftp/tsg_ran/WG4_Radio/TSGR4_AHs/TSGR4_NR_Jan2017/Docs/R4-1700095.zip.

[41] C. Carlson, "How i made wine glasses from sunflowers," *Wolfram blog*, 2011, available at https://blog.wolfram.com/2011/07/28/how-i-made-wine-glasses-from-sunflowers/.

[42] J. Krupka, "Measurements of the complex permittivity of low loss polymers at frequency range from 5 ghz to 50 ghz," *IEEE Microwave and Wireless Components Letters*, vol. 26, no. 6, pp. 464–466, Jun. 2016.

[43] G. Phillips and P. Williams, *Handbook of Hydrocolloids*. Woodhead Publishing Limited, 08 2000.

[44] *TX products data sheet and mixing instruction*, Oil center research LLC, Lafayette, LA, USA, 2016.

[45] W. Wu and C. E. Smith, "Dielectric measurements using the hp 85070a probe," in *Proceedings IEEE Southeastcon '92*, vol. 1, Apr. 1992, pp. 83–86.

[46] D. K. Misra, "A quasi-static analysis of open-ended coaxial lines (short paper)," *IEEE Transactions on Microwave Theory and Techniques*, vol. 35, no. 10, pp. 925–928, Oct. 1987.

[47] S. R. Saunders and S. R. Simon, *Antennas and Propagation for Wireless Communication Systems*, 1st ed. New York, NY, USA: John Wiley & Sons, Inc., 1999.

[48] R. J. P. Douville and D. S. James, "Experimental study of symmetric microstrip bends and their compensation," *IEEE Transactions on Microwave Theory and Techniques*, vol. 26, no. 3, pp. 175–182, Mar 1978.

A How to make skin material

This is manual for manufacturing skin material presented in this thesis at chapter 4.1.3. The chapter tells technical aspect of skin material and this guide focuses on manufacturing. Recipe is same shown in chapter and it is scaled 11.13 times bigger.

Needed equipment and materials are: kettle (metallic bowl), hot plate, scale, thermometer, plastic or metallic stirrer and (plastic) cups for scaling.

First we need to measure 1113 g deionized water to the kettle.

Next we measure 35 g of agar. Agar is added to the water

Water needs to be stirred while agar is added to avoid lumping

Next TX-151 is scaled and added to the water

When Agar and TX-151 is dissolved to the water we start heating the solution

Temperature of the solution needs to be increased to 80 ˚C. TX-151 makes solution thick and hard to stir. TX-151 can also be added to hot solution but it will lump easier. If we have old skin material it can be added to the solution during the heating

While solution is heating up we can scale 400 g polyethylene powder. In the picture we see that we scaled 413 g but that is because scale is calibrated for one cup and other cup weight ~13 g

Polyethylene powder is added in few batches to the solution to avoid spilling

When all the polyethylene is mixed to the material we can cask it and cover it with plastic while material is cooling

B Free space radiation patterns

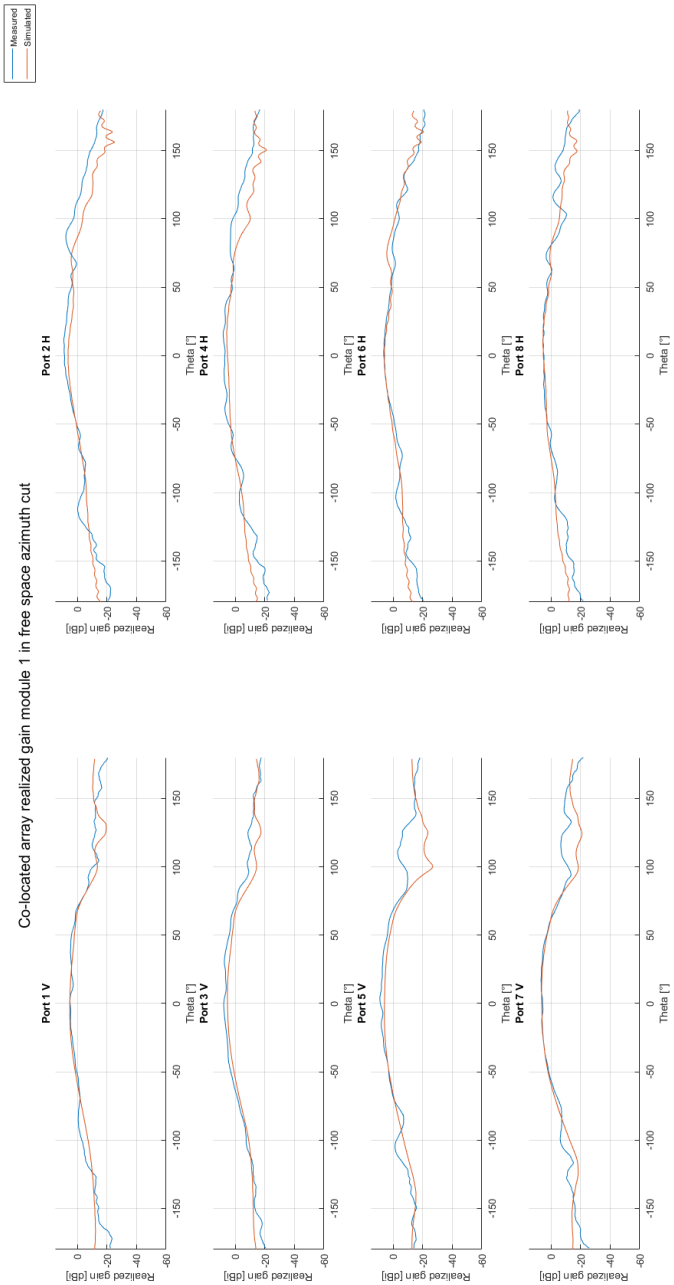

Figure B1: Azimuth cuts of module 1 of the co-located array in free space

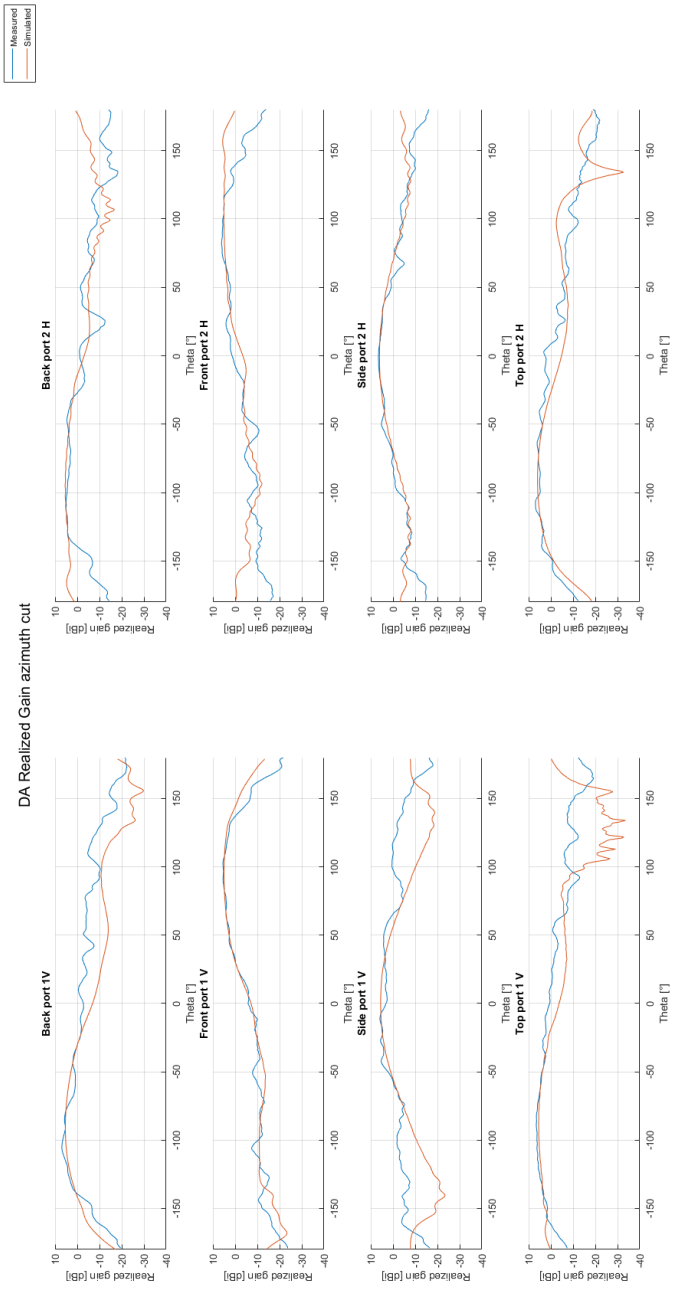

Figure B2: Azimuth cuts of module 1 of the distributed array in free space

C Phantom radiation patterns

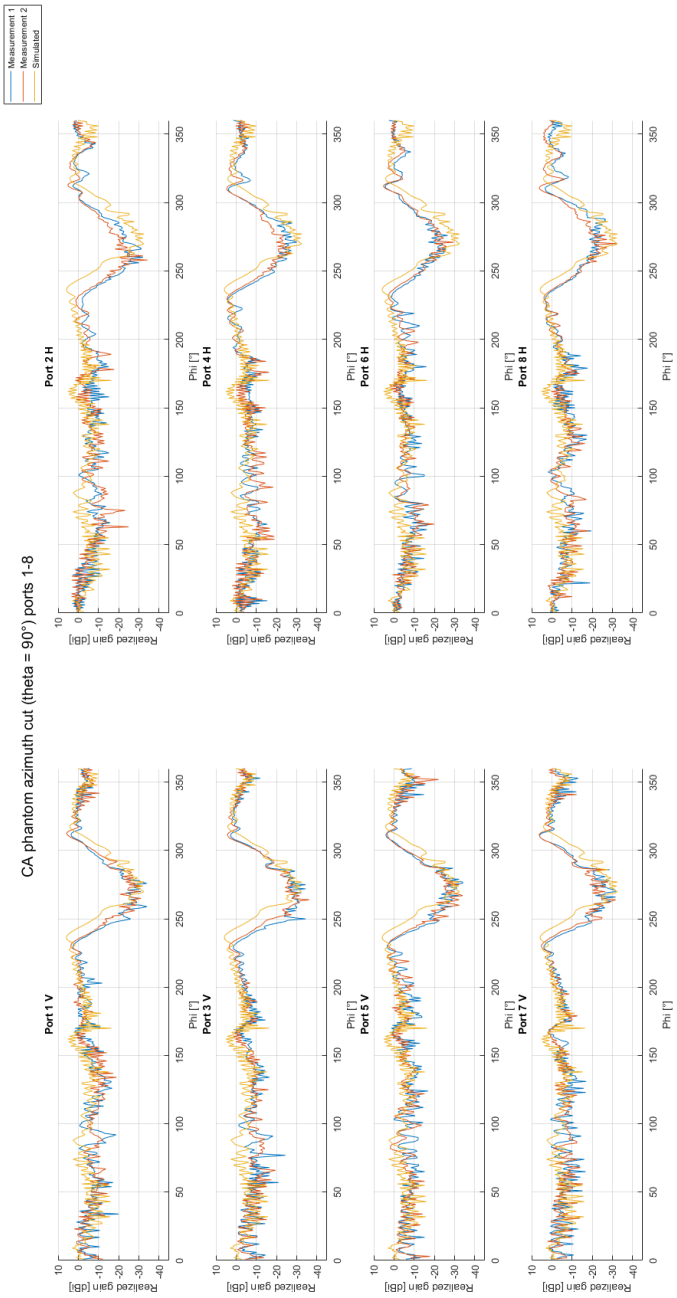

Figure C1: Azimuth cuts of module 1 of the co-located array with phantom

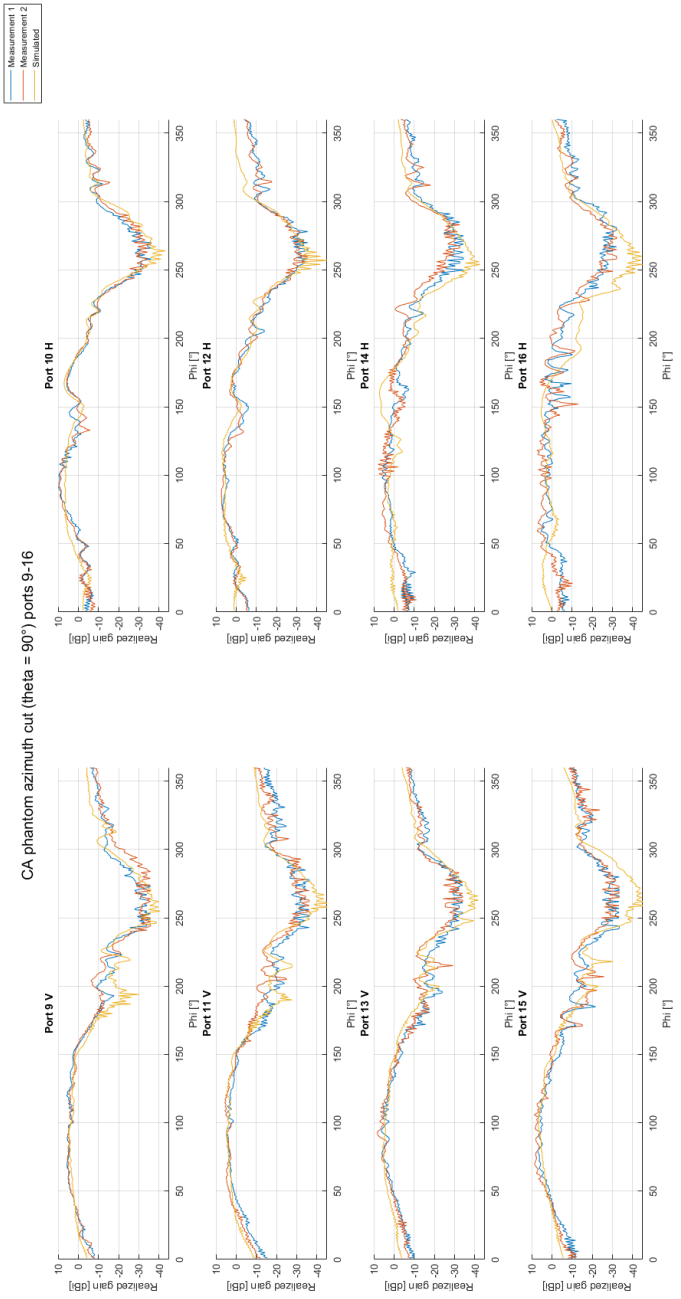

Figure C2: Azimuth cuts of module 2 of the co-located array with phantom

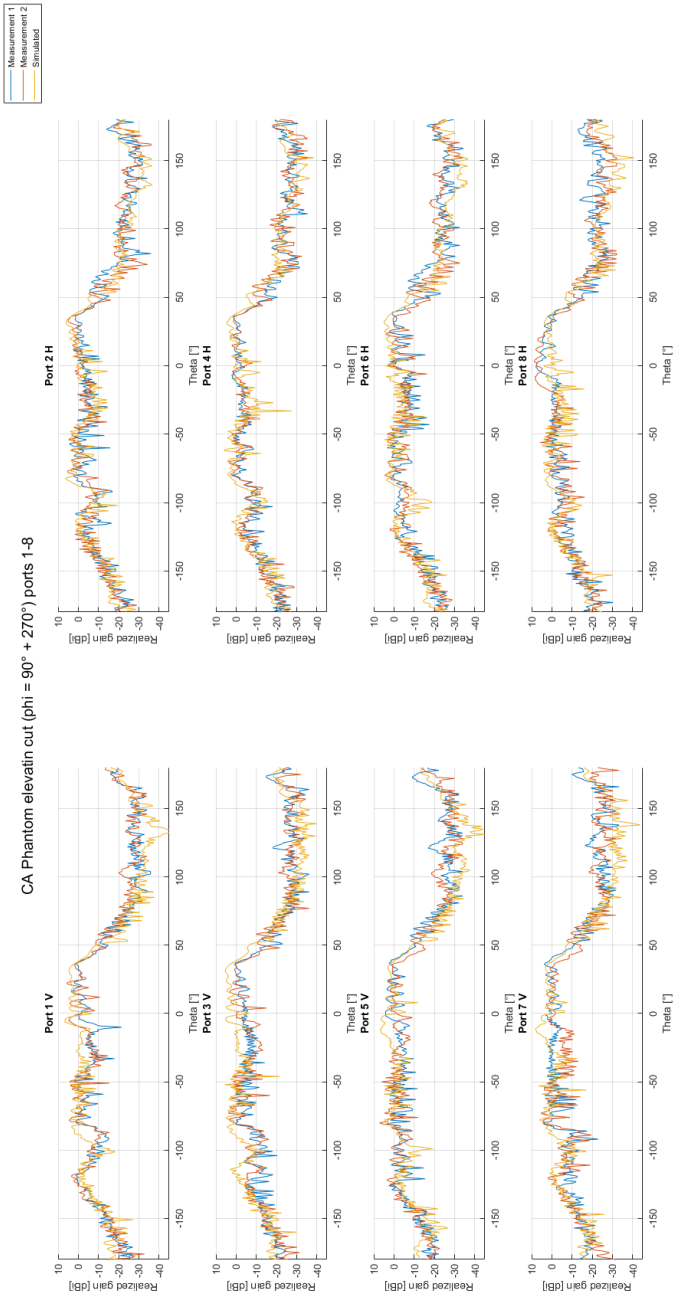

Figure C3: Elevation cuts of module 1 of the co-located array with phantom

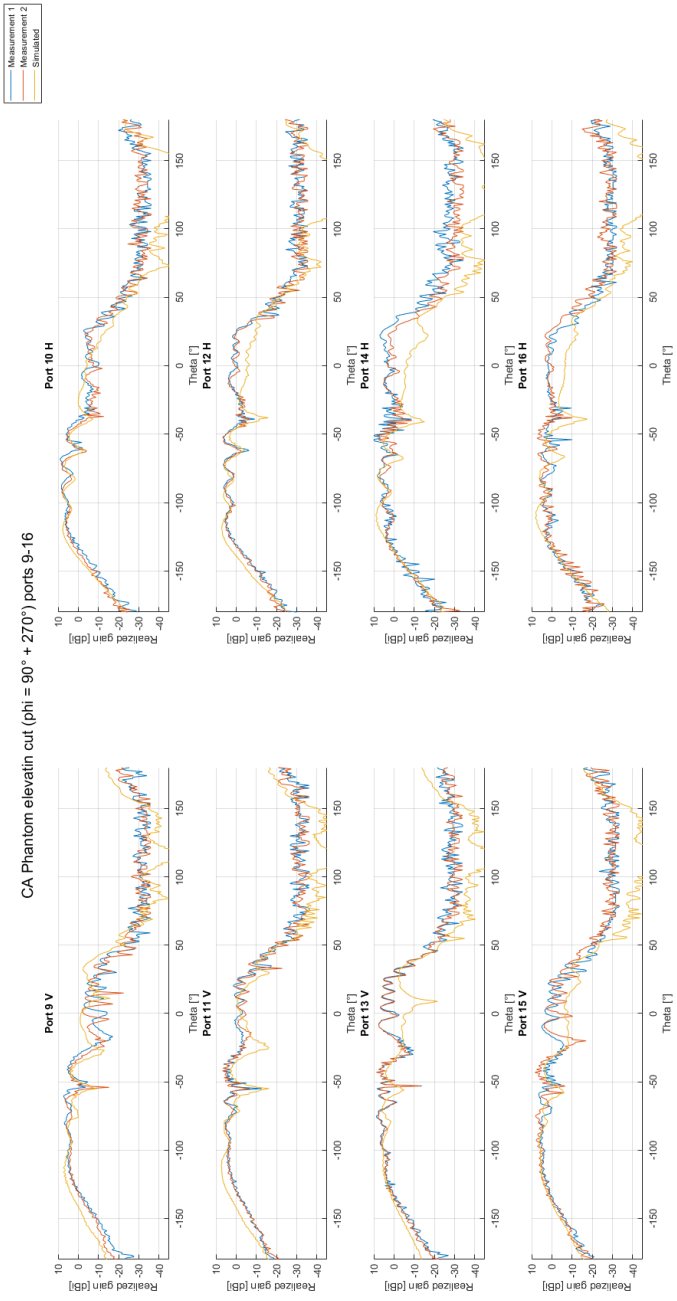

Figure C4: Elevation cuts of module 2 of the co-located array with phantom

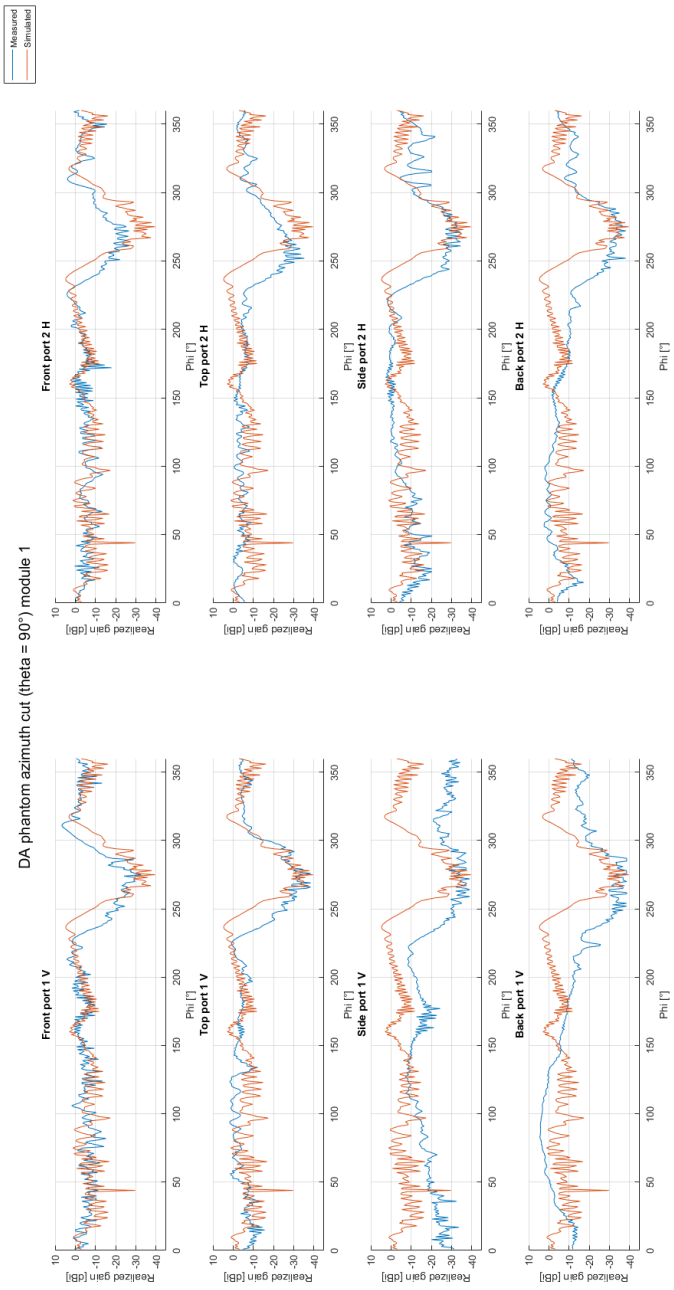

Figure C5: Azimuth cuts of module 1 of the distributed array with phantom

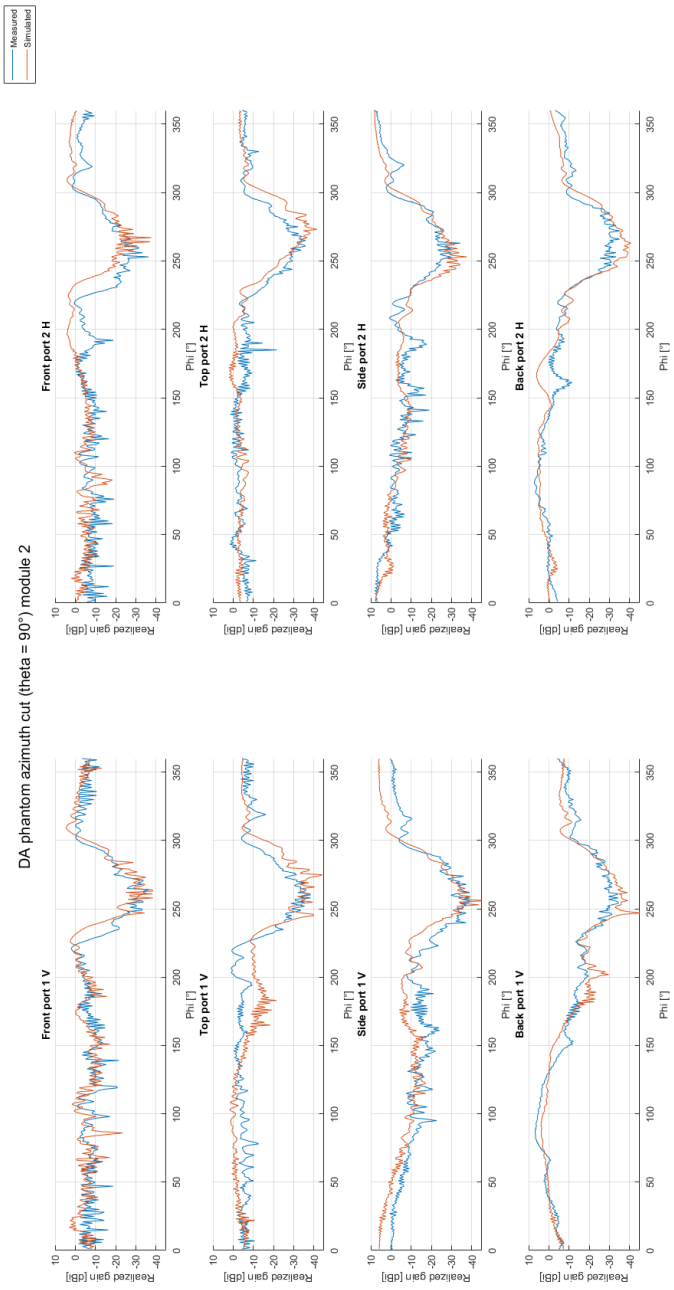

Figure C6: Azimuth cuts of module 2 of the distributed array with phantom

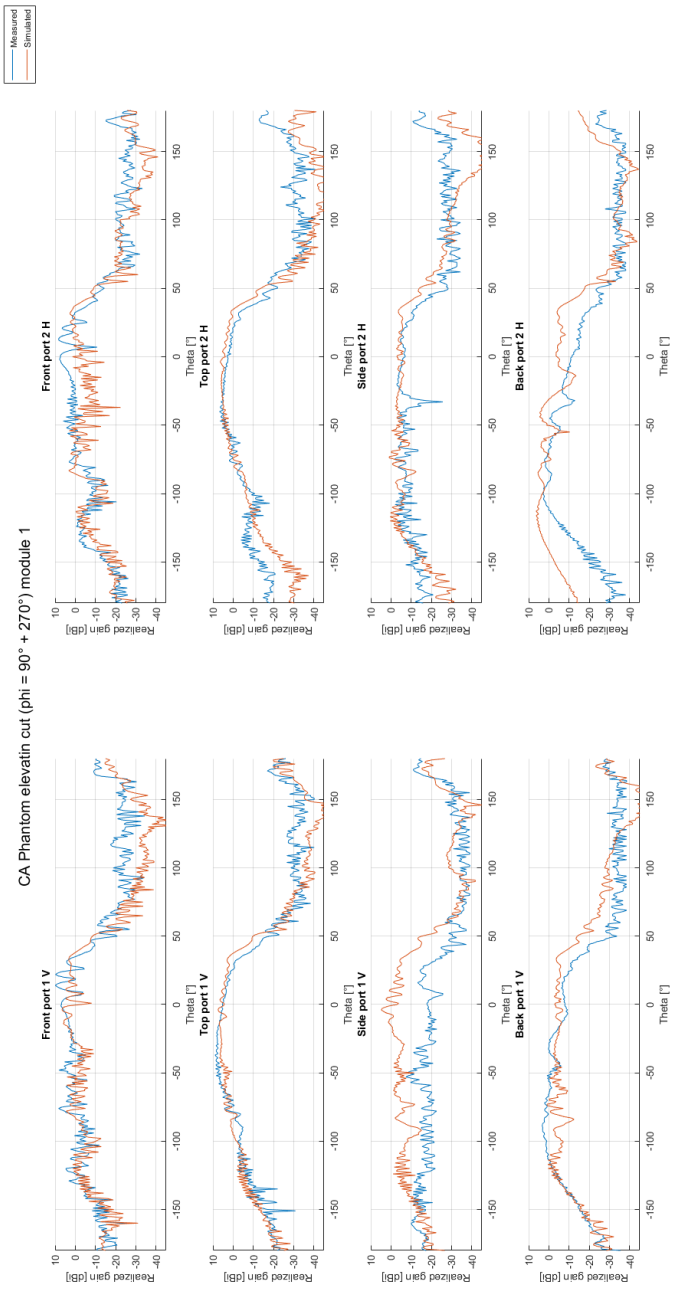

Figure C7: Elevation cuts of module 1 of the distributed array with phantom

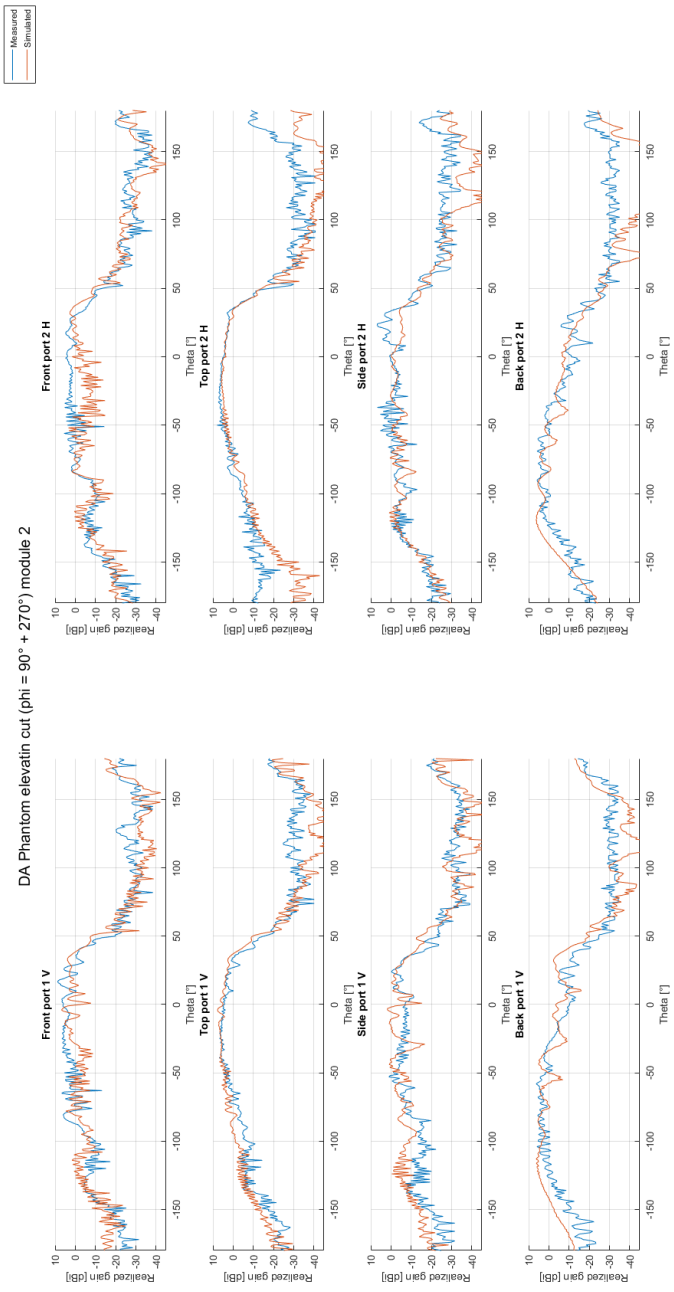

Figure C8: Elevation cuts of module 2 of the distributed array with phantom